Journal of Turbulence

ISSN: (Print) 1468-5248 (Online) Journal homepage: http://www.tandfonline.com/loi/tjot20

Zonal PANS: evaluation of different treatments of the RANS–LES interface

L. Davidson

To cite this article: L. Davidson (2016) Zonal PANS: evaluation of different treatments of the RANS–LES interface, Journal of Turbulence, 17:3, 274-307, DOI: 10.1080/14685248.2015.1093637

To link to this article: http://dx.doi.org/10.1080/14685248.2015.1093637

Published online: 22 Jan 2016.

JOURNAL OF TURBULENCE, 2016
VOL. 17, NO. 3, 274–307
http://dx.doi.org/10.1080/14685248.2015.1093637

Taylor & Francis
Taylor & Francis Group

Zonal PANS: evaluation of different treatments of the RANS–LES interface

L. Davidson

Division of Fluid Dynamics, Department of Applied Mechanics, Chalmers University of Technology, Gothenburg, Sweden

ABSTRACT

The partially Reynolds-averaged Navier–Stokes (PANS) model can be used to simulate turbulent flows either as RANS, large eddy simulation (LES) or DNS. Its main parameter is f_k whose physical meaning is the ratio of the modelled to the total turbulent kinetic energy. In RANS $f_k = 1$, in DNS $f_k = 0$ and in LES f_k takes values between 0 and 1. Three different ways of prescribing f_k are evaluated for decaying grid turbulence and fully developed channel flow: $f_k = 0.4$, $f_k = k_{\text{tot}}^{3/2}/\varepsilon$ and, from its definition, $f_k = k/k_{\text{tot}}$ where k_{tot} is the sum of the modelled, k, and resolved, k_{res}, turbulent kinetic energy. It is found that the $f_k = 0.4$ gives the best results. In Girimaji and Wallin, a method was proposed to include the effect of the gradient of f_k. This approach is used at RANS– LES interface in the present study. Four different interface models are evaluated in fully developed channel flow and embedded LES of channel flow: in both cases, PANS is used as a zonal model with $f_k = 1$ in the unsteady RANS (URANS) region and $f_k = 0.4$ in the LES region. In fully developed channel flow, the RANS– LES interface is parallel to the wall (horizontal) and in embedded LES, it is parallel to the inlet (vertical). The importance of the location of the horizontal interface in fully developed channel flow is also investigated. It is found that the location – and the choice of the treatment at the interface – may be critical at low Reynolds number or if the interface is placed too close to the wall. The reason is that the modelled turbulent shear stress at the interface is large and hence the relative strength of the resolved turbulence is small. In RANS, the turbulent viscosity – and consequently also the modelled Reynolds shear stress – is only weakly dependent on Reynolds number. It is found in the present work that it also applies in the URANS region.

ARTICLE HISTORY
Received 21 March 2015
Accepted 3 September 2015

KEYWORDS
LES; PANS; 2G-RANS; zonal model; embedded LES; hybrid RANS–LES; RANS–LES interface condition

1. Introduction

Large eddy simulation (LES) is very expensive in wall-bounded flow. To be able to extend LES to high Reynolds number, many proposals have been made in the literature to combine LES with unsteady Reynolds-Averaged Navier-Stokes (URANS) near the walls. The first and the most common method is detached eddy simulation (DES).[4–6] Later, other researchers have proposed hybrid LES–RANS [7,8] and scale-adapted simulations (SAS) [9,10]; for a review, see [11]. DES and hybrid LES–RANS use the cell size as the

CONTACT L. Davidson lada@chalmers.se

subgrid-scale (SGS) length scale. SAS does not use the cell size (except as a limiter) but uses the von Kármán length scale instead.

The main object of the methods mentioned above is that they reduce the turbulent viscosity in the LES region. There are three options to achieve this.

(1) The turbulent viscosity, ν_t, is reduced by modifying its formulation.
(2) The dissipation term in the equation for the modelled, turbulent kinetic energy, k, is increased by decreasing the turbulent length scale.
(3) The destruction term in the length scale equation (ε or ω) is decreased. This increases the dissipation term in the k equation as well as decreases the turbulent viscosity directly, since ε (or ω) appears in the denominator of the expression for ν_t.

DES [12] is based on the first option. X-LES [13] and the one-equation hybrid LES–RANS [8,14] use option number two: ν_t is decreased and the dissipation term in the k equation is increased. The third option is used in the partially averaged Navier– Stokes (PANS) model [1] and the partially integrated transport model (PITM).[15,16] PANS is used as a zonal LES–RANS method in the present work where RANS is used near the walls and LES is employed further away from the walls. We will also use PANS in embedded LES.

Much work has been presented on embedded LES lately. Menter et al. [17] present embedded LES of channel flow and the hump flow. They use the SST–RANS model upstream of the embedded LES interface. Downstream of the interface they use the model of Shur et al. [6] which consists of the Smagorinsky model in the LES region and a mixing-length model in the RANS region. At the interface, the modelled turbulence is converted into resolved turbulence using synthetic turbulence from a vortex method.[18]

Shur et al. [19] proposed a new recycling method in a interface zone between RANS and LES. The RANS and LES zones overlap and identical grids are used in the overlap region. Only the fluctuating components are recycled since the mean components are available in the entire overlap zone. They evaluated the method for flat-plate boundary flow and flow over a two-dimensional (2D) airfoil.

Poletto et al. [20] made embedded LES of the hump flow. They used delayed detached eddy simulation (DDES) in the entire region (both upstream and downstream of the interface). At the LES interface, they added synthetic fluctuations from the divergence-free synthetic eddy method.[21]

Gritskevich et al. [22] used the improved delayed detached eddy simulation (IDDES) to make embedded LES of the hump flow. They first computed the entire flow with 2D RANS. Then, they used the RANS solution to prescribe the inlet mean velocity profile at the embedded LES interface. The modelled k was taken from the RANS solution and ω was computed from k and the grid size. Synthetic fluctuations were generated with a synthetic turbulence generator.[23]

Shur et al. [24] present embedded LES of the flow over a hump. They used overlapping RANS and IDDES in the embedded interface region. At the interface, they added synthetic turbulence. They show very good agreement with measurement data.

Xiao and Jenny [25] presented a novel method for treating the RANS–LES interface in hybrid LES–RANS. They solved the RANS and LES equations in the entire domain. The RANS mesh in the LES region does not need to be the same as the LES mesh and vice versa. Drift forces were added in the overlapping regions.

As mentioned above, the PANS model is in the present work used as a zonal hybrid LES–RANS model. f_k is set to one in the RANS regions, and it is set to 0.4 in the LES region. The

interface between the RANS and LES regions is defined along a grid plane, an approach also chosen in ZDES.[26] As an alternative to using a constant f_k in the LES region, f_k can be computed using the cell size and the integral length scale, $k_{\text{tot}}^{3/2}/\varepsilon$,[2] where k_{tot} is the sum of the resolved and the modelled turbulent kinetic energy, i.e. $k_{\text{tot}} = k_{\text{res}} + k$. The reason why f_k is not computed in the present study is that it has been shown that a constant $f_k = 0.4$ works well in the LES region [27–30]; it was even shown in [30] that using constant $f_k = 0.4$ works better than computing f_k, not to mention that it is numerically more stable. Section 4 compares three alternatives ($f_k = 0.4$, computing f_k according to the equation above, and computing f_k from its definition k/k_{tot}) for decaying homogeneous grid turbulence and fully developed channel flow. It should be mentioned that Basara et al. [2] have shown that computing f_k works well when using the k–ε–ζ–f model.

In [3], a method was proposed to include the effect of the gradient of f_k. The gradient appears because the PANS filtering operation does not commute with the the spatial gradient. At RANS–LES interfaces, the spatial gradient of f_k is large. The approach of Girimaji and Wallin [3] is further developed in the present study and it is used at RANS–LES interfaces.

The appearance of the gradient of f_k at RANS–LES interfaces is similar to the method for treating RANS–LES interfaces in Hamba.[31] He shows that when the filter size varies, an additional term appears because the filtering and the spatial gradients do not commute. The divergence of a flux, q_i, for example, will include an additional term

$$\overline{\frac{\partial q_i}{\partial x_i}} = \frac{\partial \bar{q}_i}{\partial x_i} - \frac{\partial \Delta}{\partial x_i}\frac{\partial \bar{q}_i}{\partial \Delta}. \tag{1}$$

Chaouat and Schiestel [32] used the approach in [31] to modify their PITM approach. They derived the modified transport equations including commutation terms as in Equation (1). The gradients of the filter width, Δ, was replaced with gradient of the cut-off wave number, κ_c, which appear in the PITM approach. The method proposed by Hamba [31] was recently further developed and evaluated by Davidson [33] at RANS–LES interfaces using the PDH k–ω model.[34]

The modified approach of including the effect of the gradient of f_k is in the present study evaluated in fully developed channel flow and embedded LES of channel flow; in both cases, PANS is used as a zonal model. In fully developed channel flow, the RANS–LES interface is parallel to the wall and in embedded LES it is parallel to the inlet.

When the RANS–LES interface is parallel to the wall, the term including the gradient of f_k across the interface can be both positive and negative (because v' is both positive and negative). This term is included only when it reduces the modelled turbulence. Hence, the term can be seen as a *forcing* term which represents backscatter. It is used to stimulate the growth of the resolved turbulence in the LES region adjacent to the RANS region. The present method reduces the grey area problem described in [35].

The paper is organised as follows. The next section describes the equations and the interface models. The following section describes the numerical method. Then, there is a section comparing three different ways of treating f_k, followed by a section which presents and discusses the results. The final section presents the conclusions.

2. The PANS model

The low-Reynolds number PANS (LRN PANS) turbulence model reads [27]

$$\begin{aligned}
\frac{Dk}{Dt} &= \frac{\partial}{\partial x_j}\left[\left(\nu + \frac{\nu_t}{\sigma_{ku}}\right)\frac{\partial k}{\partial x_j}\right] + P_k + P_{k_{tr}} - \varepsilon,\\
\frac{D\varepsilon}{Dt} &= \frac{\partial}{\partial x_j}\left[\left(\nu + \frac{\nu_t}{\sigma_{\varepsilon u}}\right)\frac{\partial \varepsilon}{\partial x_j}\right] + C_{\varepsilon 1}P_k\frac{\varepsilon}{k} - C^*_{\varepsilon 2}\frac{\varepsilon^2}{k},\\
\nu_t &= C_\mu f_\mu \frac{k^2}{\varepsilon},\ P_k = 2\nu_t \bar{s}_{ij}\bar{s}_{ij},\ \bar{s}_{ij} = \frac{1}{2}\left(\frac{\partial \bar{u}_i}{\partial x_j} + \frac{\partial \bar{u}_j}{\partial x_i}\right),\\
C^*_{\varepsilon 2} &= C_{\varepsilon 1} + \frac{f_k}{f_\varepsilon}(C_{\varepsilon 2}f_2 - C_{\varepsilon 1}),\ \sigma_{ku} \equiv \sigma_k\frac{f_k^2}{f_\varepsilon},\ \sigma_{\varepsilon u} \equiv \sigma_\varepsilon\frac{f_k^2}{f_\varepsilon},\\
\sigma_k &= 1.4,\ \sigma_\varepsilon = 1.4,\ C_{\varepsilon 1} = 1.5,\ C_{\varepsilon 2} = 1.9,\ C_\mu = 0.09,\ f_\varepsilon = 1,
\end{aligned} \tag{2}$$

where $D/Dt = \partial/\partial t + \bar{u}_j\partial/\partial x_j$ denotes the material derivative. The damping functions are defined as

$$\begin{aligned}
f_2 &= \left[1 - \exp\left(-\frac{y^*}{3.1}\right)\right]^2\left\{1 - 0.3\exp\left[-\left(\frac{R_t}{6.5}\right)^2\right]\right\},\\
f_\mu &= \left[1 - \exp\left(-\frac{y^*}{14}\right)\right]^2\left\{1 + \frac{5}{R_t^{3/4}}\exp\left[-\left(\frac{R_t}{200}\right)^2\right]\right\},\\
R_t &= \frac{k^2}{\nu\varepsilon},\quad y^* = \frac{U_\varepsilon y}{\nu},\quad U_\varepsilon = (\varepsilon\nu)^{1/4}.
\end{aligned} \tag{3}$$

The term $P_{k_{tr}}$ in Equation (2) is an additional term which is non-zero in the interface region because $Df_k/Dt \neq 0$. The function f_ε, the ratio of the modelled to the total dissipation, is set to one since the turbulent Reynolds number is high. f_k is set to 1 in the RANS region and to 0.4 in the LES region (in Section 4 it is also computed in the LES region).

It was shown in [30] that the k and ε equations in the LES region are in local equilibrium, i.e.

$$\langle P_k\rangle - \langle\varepsilon\rangle = 0, \tag{4}$$

$$\left\langle C_{\varepsilon 1}\frac{\varepsilon}{k}P_k\right\rangle - \left\langle C^*_{\varepsilon 2}\frac{\varepsilon^2}{k}\right\rangle = 0 \tag{5}$$

($\langle . \rangle$ denotes averaging in all homogeneous directions, i.e. t, z and, in fully developed channel flow, also x). It seems that Equations (4) and (5) cannot both be satisfied since $C_{\varepsilon 1} \neq C^*_{\varepsilon 2}$; indeed, the equations are not satisfied instantaneously for which the convective terms play an important role. Equation (5) is satisfied, but

$$C_{\varepsilon 1}\frac{\langle\varepsilon\rangle}{\langle k\rangle}\langle P_k\rangle - C^*_{\varepsilon 2}\frac{\langle\varepsilon^2\rangle}{\langle k\rangle} \neq 0. \tag{6}$$

Equations (4) and (5) are both satisfied because the correlation between ε, k^{-1} and P_k (left side of Equation (5)) is stronger than that between ε^2 and k^{-1} (right side). The correlation between the quantities on the left side is larger than that on the right side because $C^*_{\varepsilon 2} > C_{\varepsilon 1}$. For more details, see [30].

2.1. The interface condition

The commutation error in PANS was recently addressed in [3]. In PANS, the equation for the modelled turbulent kinetic energy, k, is derived by multiplying the k_{tot} equation ($k_{\text{tot}} = k_{\text{res}} + k$) by f_k. The convective term in the k equation with constant f_k is then obtained as

$$f_k \frac{Dk_{\text{tot}}}{Dt} = \frac{D(f_k k_{\text{tot}})}{Dt} = \frac{Dk}{Dt}, \tag{7}$$

where

$$f_k = \frac{k}{k_{\text{tot}}}. \tag{8}$$

Now, if f_k varies in space, we get instead

$$f_k \frac{Dk_{\text{tot}}}{Dt} = \frac{D(f_k k_{\text{tot}})}{Dt} - k_{\text{tot}} \frac{Df_k}{Dt} = \frac{Dk}{Dt} - k_{\text{tot}} \frac{Df_k}{Dt}. \tag{9}$$

Since f_k in the present work is constant in time, $Df_k/Dt = \bar{u}_i \partial f_k / \partial x_i$. The second term on the right side of Equation (9) is the commutation term: it represents (excluding the minus sign) energy transfer from resolved to modelled turbulence. It can be written (on the right side of the k equation) as

$$k_{\text{tot}} \frac{Df_k}{Dt} = (k + k_{\text{res}}) \frac{Df_k}{Dt} = k \frac{Df_k}{Dt} + \frac{\langle \bar{u}_i' \bar{u}_i' \rangle}{2} \frac{Df_k}{Dt}. \tag{10}$$

The commutation term in the k_{res} equation is the same but with opposite sign, i.e.

$$- k \frac{Df_k}{Dt} - \frac{\langle \bar{u}_i' \bar{u}_i' \rangle}{2} \frac{Df_k}{Dt}. \tag{11}$$

The question is now which term should be added to the momentum equations to get the commutation term in the k_{res} equation. We start by the second term in Equation (11). This term can be represented by the source term

$$S_i^1 = -\frac{1}{2} \bar{u}_i' \frac{Df_k}{Dt} \tag{12}$$

in the momentum equation. To show that this term corresponds to the commutation term in Equation (11), consider the momentum equation for the fluctuating velocity, $\bar{u}_i'$. Multiplying S_i^1 by $\bar{u}_i' = \bar{u}_i - \langle \bar{u}_i \rangle$ and time averaging gives the source term in the k_{res} equation

as

$$-\left\langle (\bar{u}_i - \langle \bar{u}_i \rangle) \frac{1}{2} \bar{u}_i' \frac{Df_k}{Dt} \right\rangle = -\left\langle \frac{1}{2} \bar{u}_i' \bar{u}_i' \frac{Df_k}{Dt} \right\rangle = -\frac{1}{2} \langle \bar{u}_i' \bar{u}_i' \rangle \frac{Df_k}{Dt}. \tag{13}$$

Equation (13) is equal to the time average of the second term in Equation (11) as it should.

A term corresponding to the first term in Equation (11) can be added as a source term in the momentum equation as

$$S_i^2 = -\frac{k\bar{u}_i'}{\langle \bar{u}_m' \bar{u}_m' \rangle} \frac{Df_k}{Dt}. \tag{14}$$

Multiplying S_i^2 by $\bar{u}_i'$ and time averaging gives

$$-\frac{\langle k\bar{u}_i' \bar{u}_i' \rangle}{\langle \bar{u}_m' \bar{u}_m' \rangle} \frac{Df_k}{Dt} \simeq -\langle k \rangle \frac{Df_k}{Dt}, \tag{15}$$

where we assume that the correlation between k and $\bar{u}_i'$ is weak. Equation (15) is equal to the time average of the first term in Equation (11) as it should.

In [3], the second term on the right side of Equation (9) is represented by introducing an additional turbulent viscosity, ν_{tr}, in a diffusion term in the momentum equation as

$$\frac{\partial}{\partial x_j} \left(\nu_{tr} \bar{s}_{ij} \right), \quad \bar{s}_{ij} = \frac{1}{2} \left(\frac{\partial \bar{u}_i}{\partial x_j} + \frac{\partial \bar{u}_j}{\partial x_i} \right), \tag{16}$$

where

$$\nu_{tr} = \frac{P_{k_{tr}}}{|\bar{s}|^2}. \tag{17}$$

The term, $P_{k_{tr}}$, is computed as

$$P_{k_{tr}} = k_{\text{tot}} \frac{Df_k}{Dt}. \tag{18}$$

$P_{k_{tr}}$ is an additional production term in the k equation (see Equation (2)). In [3], $P_{k_{tr}}$ is rewritten using Equation (8) as

$$P_{k_{tr}} = \frac{k}{f_k} \frac{Df_k}{Dt}. \tag{19}$$

2.2. Modelling the interface

The gradient of f_k across a RANS–LES interface gives rise to an additional term in the momentum equations and the k equation. In the present work, these terms are included only when the flow goes from a RANS region to an LES region. The effect of these terms will reduce k and act as a forcing term in the momentum equations. Four different models are investigated.

2.2.1. Interface Model 1

This is based on the approach suggested in [3]. The additional turbulent viscosity, ν_{tr}, gives an additional production term, $P_{k_{tr}}$, in the k equation (see Equation (19)). Since we are interested in stimulating resolved turbulence in the LES region adjacent to the RANS region, only negative values of ν_{tr} are included. A negative ν_{tr} means physically transfer of kinetic energy from modelled to resolved. It is found that the magnitude of the positive values of ν_{tr} is actually larger than the magnitude of the negative ones, which means that $\langle \nu_{tr} \rangle > 0$. The negative values correspond to $Df_k/Dt < 0$ (see Equations (17)–(19)), i.e. when a fluid particle in a RANS region passes the interface into an adjacent LES region. However, ν_{tr} takes such large (negative) values that $\nu_t + \nu_{tr} < 0$. To stabilise the simulations, it was found necessary to introduce a limit $\nu_t + \nu_{tr} > 0$ in the diffusion term in the momentum equation. No such limit is used in the k equation, and hence $P_k + P_{k_{tr}}$ is allowed to go negative.

2.2.2. Interface Model 2

This model is identical to Model 1 except that Equation (18) is used instead of Equation (19). k_{tot} in Equation (18) is defined as

$$k_{\text{tot}} = k + \frac{1}{2}\langle \bar{u}_i' \bar{u}_i' \rangle_{\text{r.a}} \tag{20}$$

where subscript r.a denotes running average. Is is averaged in all homogeneous directions including time (note that time is not a homogeneous direction in decaying grid turbulence, see Section 4.1). Since k_{tot} is mostly larger than k/f_k,[30] this approach will give a larger magnitude of the (negative) production than Model 1. It will be seen that this modification is of utmost importance.

2.2.3. Interface Model 3

The right side of Equation (10) is added to the k equation, but only when the flow goes from a RANS region to an LES region (i.e. $Df_k/Dt < 0$), i.e.

$$P_{k_{tr}} = k_{\text{tot}} \min\left(\frac{Df_k}{Dt}, 0\right) \tag{21}$$

where k_{tot} is computed as in Equation (20). The production term $P_{k_{tr}} < 0$ which means that it reduces k as it should. The sum of the S_i^1 and S_i^2 terms (see Equations (12) and (14)) in the momentum equations read

$$S_i = -\min\left(\frac{Df_k}{Dt}, 0\right)\left(0.5 + \frac{k}{\langle \bar{u}_m' \bar{u}_m' \rangle_{r.a.}}\right)\bar{u}_i'. \tag{22}$$

Since $Df_k/Dt < 0$, the source S_i has the same sign as $\bar{u}_i'$; this means that the source enhances the resolved turbulence as it should.

It may be noted that Df_k/Dt in Equation (21) assumes the correct (i.e. negative) sign irrespectively of the orientation of the RANS–LES interface. Consider, for example, the RANS–LES interfaces at the lower and upper walls in fully developed channel flow (Figure 1). For these interfaces, the gradient of f_k in Equation (21) reads $\bar{v}\,\partial f_k/\partial y$. When a fluid particle at the lower interface goes from the RANS region to the LES region, $\bar{v} > 0$ and $\partial f_k/\partial y < 0$,

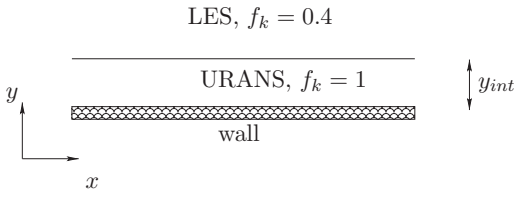

Figure 1. Fully developed channel flow: the URANS and LES regions.

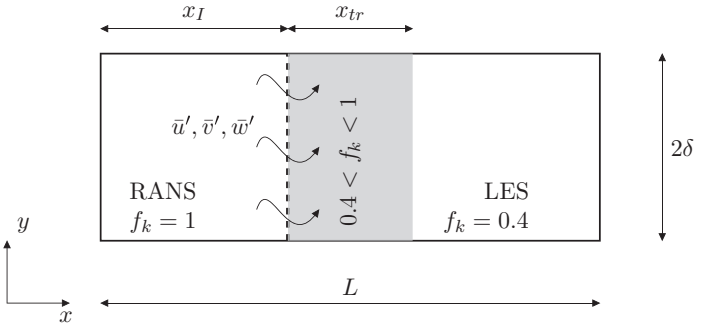

Figure 2. Embedded LES. The vertical thick line shows the interface at $x_I = 0.95$. f_k varies linearly in the grey area (width x_{tr}) from 1 to 0.4. $\delta = 1$.

so that $\bar{v}\partial f_k/\partial y < 0$ as intended. Also, for the upper interface, we get $\bar{v}\partial f_k/\partial y < 0$ since $\bar{v} < 0$ and $\partial f_k/\partial y > 0$. For non-Cartesian grids, the material derivative, $Df_k/Dt < 0$, has to be formulated in local grid coordinates.

It is, however, found that the forcing often becomes too strong when S_i is added to the momentum equation. The effect of adding or neglecting S_i in the momentum equations is evaluated in Section 5.

The differences between Models 3 and 2 are that:

- When $S_i = 0$, no explicit modification is made in the momentum equation in Model 3 (recall that $-\nu < \nu_{tr} < 0$ is used in the momentum equation in Models 1 and 2).
- Model 2 (and Model 1) may need regularisation in case $|\bar{s}| \to 0$ in the denominator of $\nu_{t_{tr}}$ in Equation (18). No such regularisation, however, is used in the present work. It can be argued that the commutation term in Model 3 is introduced in a more physical way compared to Models 1 and 2 where artificially negative viscosities are used.

2.2.4. Interface Model 4

This interface model was developed in [30] for horizontal interfaces. The modelled turbulent kinetic energy in the LES region adjacent to the interface is reduced by setting the usual convection and diffusion fluxes of k at the interface to zero. New fluxes are introduced in which the interface condition is set to $k_{\text{int}} = f_k k_{\text{RANS}}$ ($f_k = 0.4$), where k_{RANS} is the k value in the cell located in the URANS region adjacent to the interface. No modification is made for the convection and diffusion of ε across the interface. The implementation is presented in some detail later. We write the discretised equation in the y direction (see Figures 1 and 2) as follows [36]:

$$a_P k_P = a_N k_N + a_S k_S + S_U, \quad a_P = a_S + a_N - S_P$$

where a_S and a_N include to the convection and diffusion through the south and north faces, respectively, and S_U and $S_P k_P$ include the production and the dissipation term, respectively. For a cell in the LES region adjacent to the interface (cell P), a_S is set to zero, setting the usual convection and diffusion fluxes to zero. New fluxes, including f_k, are incorporated in additional source terms as

$$S_U = (C_s + D_s) f_k k_S, \quad S_P = -(C_s + D_s)$$
$$C_s = \max(\bar{v}_s A_s, 0), \quad D_s = \frac{\mu_{\text{tot}} A_s}{\Delta y}, \tag{23}$$

where C_s and D_s denote convection (first-order upwind) and diffusion, respectively, through the south face, and A_s is the south area of the cell. As can be seen, the k_S is multiplied by f_k and hence the new convective flux is a factor f_k smaller than the original one. Also, the diffusion flux is smaller; it is $D_s(f_k k_S - k_P)$ compared with the original flux $D_s(k_S - k_P)$.

The treatment of the k equation for a vertical interface (the embedded interface in the channel flow) is exactly the same as for a horizontal interface. The difference is that an interface condition is needed also for the ε equation which reads [28]

$$\varepsilon_I = C_\mu^{3/4} \frac{k_I^{3/2}}{\ell_{\text{sgs}}}, \quad \Delta = V^{1/3}, \quad C_S = 0.1, \quad \ell_{\text{sgs}} = C_S \Delta, \tag{24}$$

where subscript I denotes inlet or interface; V is the volume of the cell. The sensitivity to the value of the Smagorinsky coefficient, C_S, was investigated in [30] and was found to be weak.

3. Mean flow equations and numerical method

The momentum equations with an added turbulent viscosity reads

$$\frac{\partial \bar{u}_i}{\partial t} + \frac{\partial \bar{u}_j \bar{u}_i}{\partial x_j} = \delta_{1i} - \frac{1}{\rho}\frac{\partial \bar{p}}{\partial x_i} + \frac{\partial}{\partial x_j}\left((\nu + \nu_t)\frac{\partial \bar{u}_i}{\partial x_j}\right) + S_i, \tag{25}$$

where the first term on the right side is the driving pressure gradient in the streamwise direction, which is used only in the fully developed channel flow simulations. The last term on the right side is the additional source term in Model 3 (see Equation (22)). The effect of this term is shown in Figures 15 and 25.

An incompressible, finite volume code is used.[7] The numerical procedure is based on an implicit, fractional step technique with a multigrid pressure Poisson solver and a non-staggered grid arrangement. For the momentum equations, second-order central differencing is used for the fully developed channel flow. For the embedded channel flow, we use the second-order upwind [37] scheme in the RANS region upstream of the interface and second-order central differencing in the LES region downstream of the interface. The Crank–Nicolson scheme is used in the time domain and the first-order hybrid central/upwind scheme is used in space for solving the k and ε equations.

4. Should f_k be constant or should it be computed?

The physical meaning of f_k is the ratio of modelled to total turbulent kinetic energy (see Equation (8)). Hence it is expected that it should be smaller when the grid is refined. One way to compute f_k is as proposed by [2]

$$f_k = C_\mu^{-1/2} \left(\frac{\Delta}{L_t} \right)^{2/3}, \quad L_t = \frac{k_{\text{tot}}^{3/2}}{\varepsilon}, \quad \Delta = (\Delta V)^{1/3}. \tag{26}$$

Kenjeres and Hanjalic [38] have made a slightly different proposal which reads

$$f_k = \frac{\Delta}{L_t}. \tag{27}$$

This expression was found to give far too small f_k and hence the formula in Equation (26) was chosen for evaluation.

Since the running average of k_{tot} is computed in Models 2 and 3, the option of computing f_k from its definition is also evaluated, i.e.

$$f_k = \frac{k}{k_{\text{tot}}} \tag{28}$$

where k_{tot} is computed using the running average (see Equation (20)); the instantaneous value of k is used.

In this section, we evaluate the difference between computing f_k from Equation (26) or Equation (28), or using constant $f_k = 0.4$ in the LES regions. For comparison, the results using the dynamic Smagorinsky model [39,40] are also included in Section 4.1.

4.1. Decaying homogeneous isotropic turbulence

The first test case is decaying homogeneous isotropic turbulence (DHIT). The computational domain is a cubic box with side length 2π. Three different meshes have been employed: 32^3, 64^3 and 128^3 cells. Periodic boundary conditions are prescribed at all boundaries.

The predictions are compared with experiments.[41] We have made the experimental data non-dimensional using the characteristic scales, $u_{\text{ref}} = (1.5u_{\text{rms},\,0})^{1/2}$ and $L_{\text{ref}} = 11M_g/(2\pi)$, where $u_{\text{rms},\,0}$ denotes the initial measured RMS fluctuation and M_g is the mesh size of the turbulence generating grid in the experiments. The turbulence spectra in the experiments were measured at three downstream locations corresponding to the times $tU_0/M_g = 42$, 98 and 171. The corresponding non-dimensional times in the simulations are 0, 0.87 and 2, respectively.

The initial velocity is obtained by inverse Fourier transformation using the measured spectrum at $tU_0/M_g = 42$. The initial velocity field is generated by a widely used computer program from the group of Prof. Strelets in St. Petersburg. Initial boundary conditions for the turbulent quantities are set as in [27], i.e. $k = f_k k_{\text{res}}$ ($f_k = 0.4$) and $\varepsilon = C_\mu^{3/4} k^{3/2}/\ell_{\text{sgs}}$ with the SGS length scale, ℓ_{sgs}, taken from the Smagorinsky model as $\ell_{\text{sgs}} = C_s\Delta$ ($C_s = 0.1$).

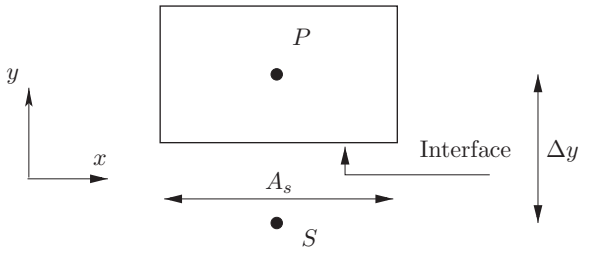

Figure 3. Control volume, *P*, in the LES region adjacent to the interface.

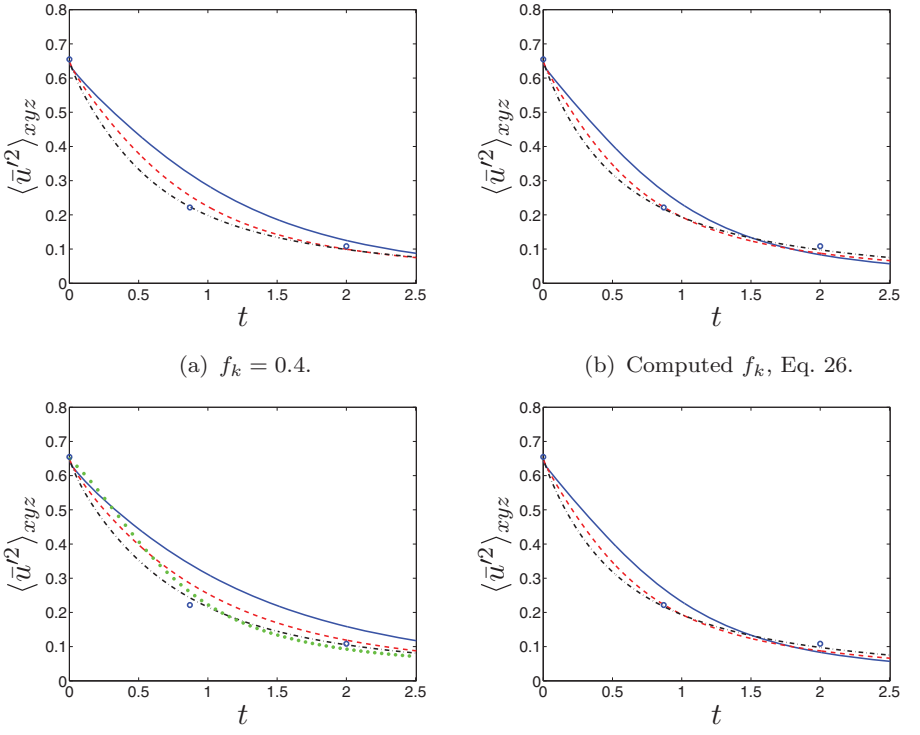

(a) $f_k = 0.4$.

(b) Computed f_k, Eq. 26.

(c) Computed $f_k = k/k_{tot}$, Eq. 28; ····: DNS, 128^3.

(d) The Dynamic Smagorinsky model.

Figure 4. DHIT, decaying turbulence. ——: 32^3; – – –: 64^3; – · –: 128^3.

Figure 3 presents the decay of resolved turbulence versus time. The predictions are compared with two experimental data at $t = 0.87$ and 2. The decay is initially stronger when f_k is computed from Equation (26) compared to $f_k = 0.4$, but at the last measurement station ($t = 2$), the two approaches give similar resolved turbulence. Computing f_k from Equation (28) gives a more consistent behaviour compared to Equation (26): the decay rate increases smoothly when the grid is refined. The decay with DNS (no model) with the 128^3 mesh is also included in Figure 4(c); DNS gives, as expected, a slightly slower decay than when computing f_k from Equation (28). The predicted decay by the dynamic model is in slightly better agreement with experiments than all PANS models. Figure 5 explains

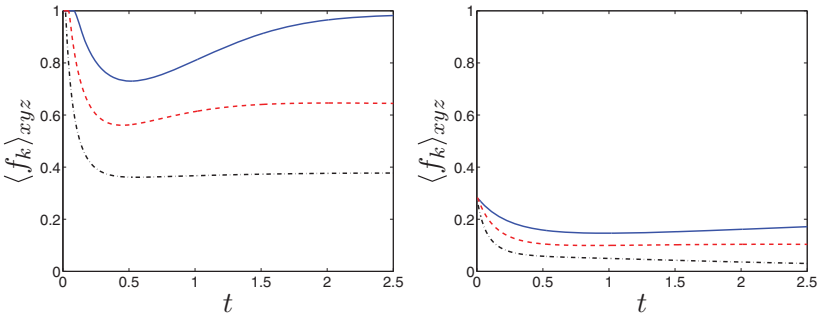

(a) Computed f_k, Eq. 26. (b) Computed $f_k = k/k_{tot}$, Eq. 28.

Figure 5. DHIT, computed f_k. ——: 32^3; – –: 64^3; – · –: 128^3.

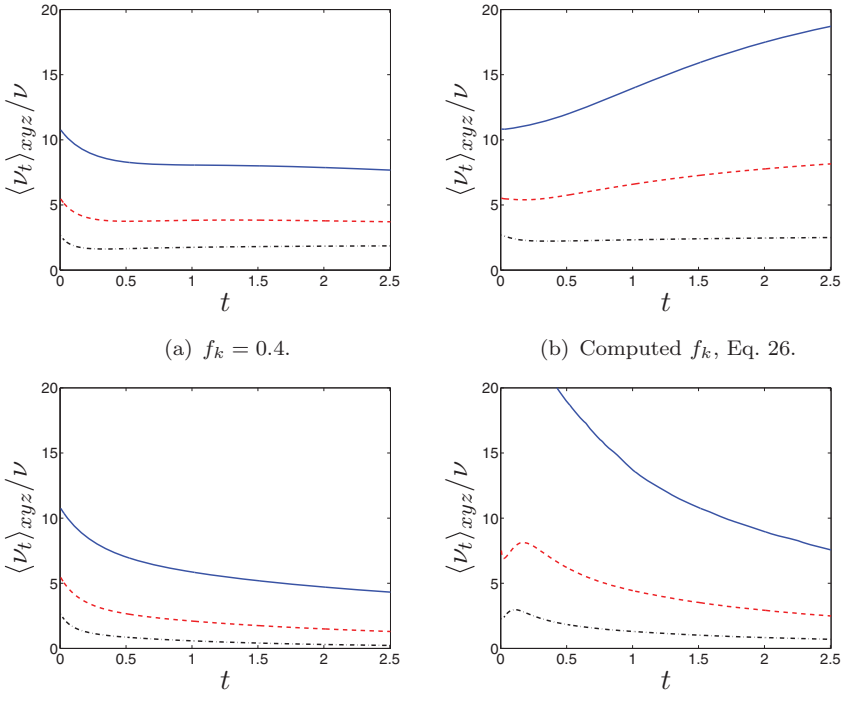

(a) $f_k = 0.4$. (b) Computed f_k, Eq. 26.

(c) Computed $f_k = k/k_{tot}$, Eq. 28. (d) The Dynamic Smagorinsky model.

Figure 6. DHIT, turbulent viscosity. ——: 32^3; – –: 64^3; – · –: 128^3.

the strong decay with the 32^3 mesh when f_k is computed using Equation (26): the reason is that the computed f_k is close to one. As expected, the finer mesh, the smaller f_k. For the 128^3 mesh, Equation (26) gives $f_k \simeq 0.4$. Computing f_k from Equation (28) gives much smaller f_k than Equation (26).

Figure 6 presents the turbulent viscosities. Considering the f_k in Figure 5, it is consistent that f_k from Equation (26) gives much larger turbulent viscosity than when using Equation (28) (with $f_k = 0.4$ between the two). f_k from Equation (28) gives even a smaller viscosity than the dynamic model on all three meshes. Furthermore, when using Equation (26),

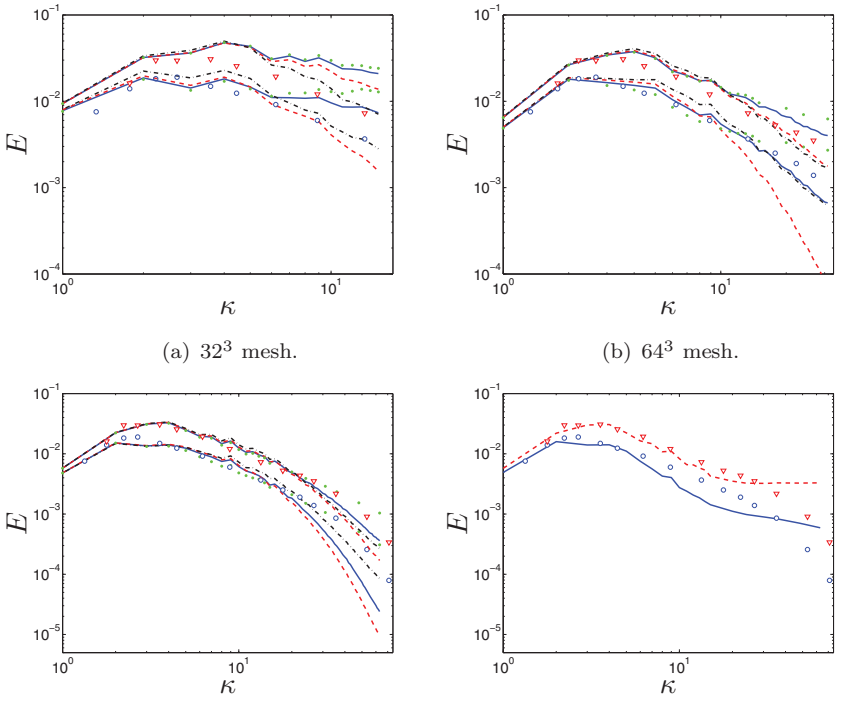

(a) 32^3 mesh. (b) 64^3 mesh.

(c) 128^3 mesh. (d) 128^3 mesh. DNS (no turbulence model).

Figure 7. DHIT, energy spectra. ▬ : $f_k = 0.4$; ▬ ▬ : computed f_k (Equation (26)); ▬ · ▬ : dynamic model; ▪▪▪ : computed $f_k = k/k_{\text{tot}}$ (Equation (28)); ▽ : $t = 0.87$; ○ : $t = 2$.

the turbulent viscosity increases with time, especially so for the coarse mesh. In RANS, the turbulent kinetic energy and its dissipation decay as $k \propto t^{-5/4}$ and $\varepsilon \propto t^{-9/4}$, respectively, so that $\nu_t \propto t^{-1/4}$, i.e. the turbulent viscosity decreases with time. We expect that the turbulent viscosity should decrease with time also in LES; this is the case for both the dynamic model, constant f_k and using Equation (28) (Figure 6(a), 6(c) and 6(d)), but not when computing f_k from Equation (26) (Figure 6(b)).

Figure 7 shows the energy spectra for the four models on the three meshes and DNS on the fine mesh. On the coarse mesh, computing f_k from Equation (26) gives slightly better agreement with experiments than $f_k = 0.4$, but on the other two meshes, $f_k = 0.4$ gives better – or much better – agreement. Comparing $f_k = 0.4$ with using Equation (28), we find that the latter model gives too small a decay at high wave numbers. The PANS simulations in Figure 7 can be summarised as follows: f_k from Equation (26) gives too large a decay at high wave numbers, f_k from Equation (28) too small a decay, and $f_k = 0.4$ in between the two. This is consistent with the turbulent viscosities in Figure 6. The spectra using the dynamic model give better agreement with experiments than all the PANS models.

For the fine mesh, the spectrum using Equation (28) gives good agreement with experiments. The PANS model is supposed to behave as DNS when f_k becomes small. f_k is indeed small for the finest mesh (see Figure 5(b)). It is, therefore, interesting to make a comparison between f_k from Equation (28) and DNS (see Figure 7(d)). It can be seen that DNS gives reasonable spectra, but the increase at high wave numbers reveals – as expected – that the

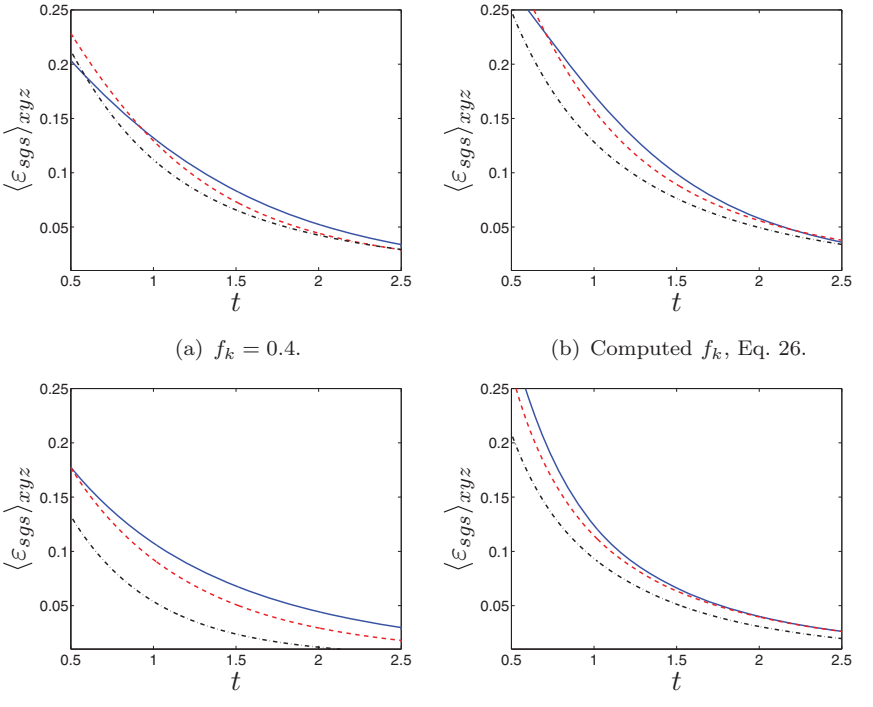

(a) $f_k = 0.4$.

(b) Computed f_k, Eq. 26.

(c) Computed $f_k = k/k_{tot}$, Eq. 28.

(d) Dynamic model.

Figure 8. DHIT, SGS dissipation, $\varepsilon_{\text{sgs}} = -\tau_{ij}\frac{\partial \bar{u}_i'}{\partial x_j}$ (τ_{ij} denotes the SGS stress tensor). ——: 32^3; – –: 64^3; – · –: 128^3.

dissipation is insufficient, i.e. the mesh is too coarse for DNS. Nevertheless, comparison between Figure 7(c) and 7(d) shows that the PANS simulations using Equation (28) and DNS are fairly similar; an even finer mesh would probably increase the similarity. Using Equation (26), the similarity with DNS is much smaller (cf. Figure 7(b) and 7(d)) and the reason is that the predicted f_k is much larger than when using Equation (28). However, if the mesh is strongly refined, it is expected that the PANS results using Equation (26) will be similar to DNS since it is expected that the mesh refinement will make f_k go towards zero (the mesh refinements from 32^3 to 128^3 do indeed reduce f_k; see in Figure 5(a)).

Finally, we plot the SGS dissipation (see Figure 8). This quantity dissipates resolved turbulent kinetic energy. According to the theory, the cut-off is located in the $-5/3$ region. Hence, when the grid is refined/coarsened and the location of cut-off moves in wave number space, the SGS dissipation should not change in theory. This means we would like our model to dissipate the same amount of turbulence as we refine/coarsen the mesh. In other words, the SGS model should be *grid-independent*. As seen in Figure 8, the constant f_k does a fairly good job in keeping ε_{sgs} constant as the grid is coarsened. Computing f_k from Equations (26) and (28) both give a larger spread in ε_{sgs} when refining the grid; the dynamics model gives a ε_{sgs} as grid-independent ε_{sgs} as $f_k = 0.4$. It may be noted that for the fine mesh, ε_{sgs} using f_k from Equation (28) goes to zero for $t > 2.1$; the reason is the small f_k (see Figure 5(b)).

Table 1 Grids. Fully developed channel flow. f_y denotes geometric stretching.

Re_τ	Δy^+	Δx^+	Δz^+	N_y	f_y
2000	2.0 – 230	200	100	80	1.13
4000	2.2 – 520	400	200	80	1.15
8000	1.5 – 1050	800	400	96	1.15

Often, we take it for granted that the turbulent viscosity should increase when the grid is coarsened. But in order to keep ε_{sgs} constant when the grid is coarsened, the finite volume method must respond in an appropriate manner and reduce the resolved velocity gradients, $\partial \bar{u}_i'/\partial x_j$ so that ε_{sgs} stays constant (for wave numbers in the $-5/3$ region $\partial \bar{u}_i'/\partial x_j \propto \Delta^{-2/3}$ and, since $\varepsilon_{\text{sgs}} \propto \Delta^0$, ν_t must be proportional to $\Delta^{4/3}$). When coarsening the grid, the key question is neither that the viscosity should increase nor that the resolved velocity gradients should decrease, but that the product of the modelled, turbulent stresses and the velocity gradient, $\varepsilon_{\text{sgs}} = -\tau_{ij}\partial \bar{u}_i'/\partial x_j$, should stay constant.

4.2. Fully developed channel flow at $Re_\tau = 8000$

The Reynolds number is defined as $Re_\tau = u_\tau \delta/\nu$ where δ denotes half-channel height. The streamwise, wall-normal and spanwise directions are denoted by x, y and z, respectively. The size of the domain is $x_{\max} = 3.2$, $y_{\max} = 2$ and $z_{\max} = 1.6$. The mesh has 32×32, 64×64 or 128×128 cells in the x–z planes. Details of the grids are given in Table 1. The location of the interface is $y^+ \simeq 500$. f_k is set to one in the RANS regions near the walls (see Figure 1). In the LES region, f_k is either set to 0.4 or it is computed from Equation (26) or (28). Model 4 (see Section 2.2.4) is used at the RANS–LES interfaces. A running average is used when computing k_{tot} (Equation (20)) in the definition of f_k. Since the simulations are always started from results obtained from earlier simulation (using, for example, another interface model), the running average is always started from the first time step. The same procedure is used when Models 2 and 3 are used in the next section. The sensitivity to running averaging for k_{tot} in evaluated in Section 5.

Figures 9–12 present the velocity profiles, the turbulent viscosities, the computed f_k and the total, turbulent kinetic energy. As can be seen, when computing f_k from Equation (26) on the coarse mesh, it attains values close to one. The result is a poorly predicted velocity profile, very large viscosities ($\langle \nu_t \rangle_{\max}/\nu \simeq 415$, not shown) in the LES region; furthermore, the resolved turbulence is zero in the entire domain. The predictions on the fine mesh are not very good either. The velocity profile near the centre on the fine mesh of the channel is somewhat over-predicted (Figure 9(b)); it seems that the turbulent viscosity gets too small in the LES region (see Figure 10(b)). Computing f_k from Equation (28) gives accurate results for the coarse grid; this is probably rather fortuitous because the turbulence viscosity is essentially zero in the LES region for all three meshes. On the medium and the fine mesh, Equation (28) predicts very poor velocity profile; the reason is the small f_k (Figure 11(b)) and consequently a very small turbulent viscosity (Figure 10(b)).

The results using Equation (26) on the coarse grid may seem somewhat surprising: we get $f_k \simeq 1$ (Figure 11(a)) in the entire region, but yet the solution does not correspond to a RANS solution as expected. The reason is the interface term (Model 4), which decreases

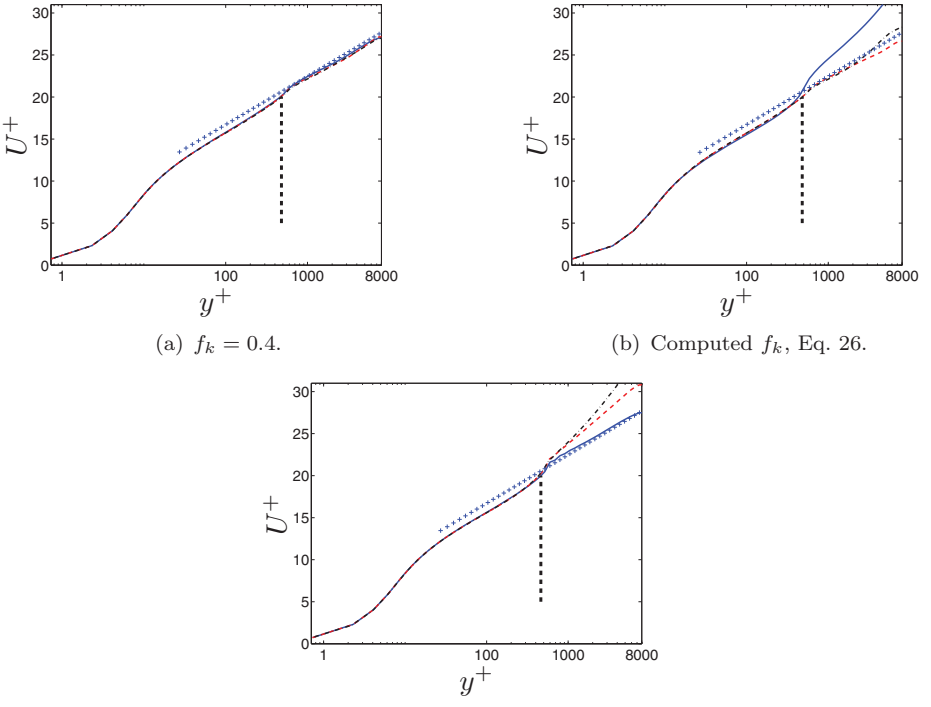

(a) $f_k = 0.4$.

(b) Computed f_k, Eq. 26.

(c) Computed f_k, Eq. 28.

Figure 9. Fully developed channel flow. $Re_\tau = 8000$. Model 4 is used at the interface. Thick vertical line shows the location of the RANS–LES interface: ——: 32^3; – –: 64^3; – · –: 128^3; +: $U^+ = \ln(y^+)/0.4 + 5.2$.

the turbulent viscosity near the RANS–LES interface (see Figure 10(b)). Without interface term, we get a steady RANS solution as expected (not shown). This is also the case when using Equation (28): without the interface term, the flow gives a steady RANS solution as it should (not shown).

Contrary to computing f_k from Equation (26) or (28), using $f_k = 0.4$ in the LES region gives velocity profiles which are in good agreement with the log law. It may be noted that the turbulent viscosity stays constant as the grid is refined; the turbulent viscosity is *grid-independent*. The is probably a big advantage when using the model in flow with complex geometries where the cell size may vary strongly. The total, turbulent kinetic energy agrees fairly well with DNS on $Re_\tau = 4200$ for all three meshes; however, it is somewhat over-predicted in the RANS region.

5. Results

In the previous section, it was found that a constant $f_k = 0.4$ in the LES region is superior compared with computing f_k from Equation (26) or (28). In the literature, there are several proposals on how to compute f_k. The proposals by Basara et al. [2] and Kenjeres and Hanjalic [38] are given in Equations (26) and (27), respectively. Other formulations are proposed by Girimaji and Abdol-Hamid [43] who compute it as $3(\Delta_{\min}/L_t)^{2/3}$, where $\Delta_{\min}$ is the smallest grid cell size and $L_t = (k + k_{\text{res}})^{3/2}/\varepsilon$. Foroutan and Yavuzkurt [44] derives

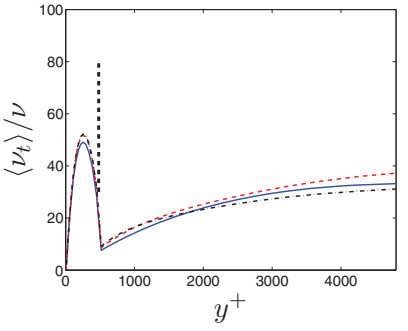

(a) $f_k = 0.4$.

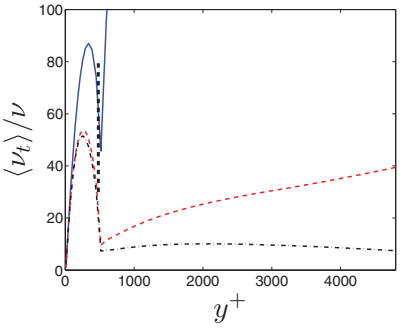

(b) Computed f_k, Eq. 26.

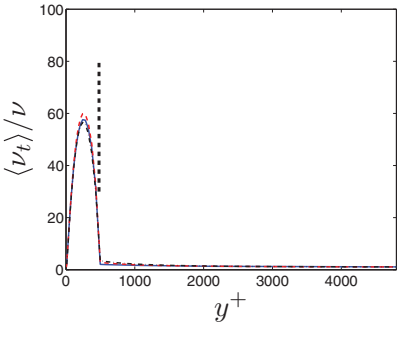

(c) Computed f_k, Eq. 28.

Figure 10. Fully developed channel flow. $Re_\tau = 8000$. Model 4 is used at the interface. ——: 32^3; – – –: 64^3; – · –: 128^3.

an expression from the energy spectrum which reads

$$f_k = 1 - \left[\frac{(\Lambda/\Delta)^{2/3}}{0.23 + (\Lambda/\Delta)^{2/3}} \right]^{9/2}. \tag{29}$$

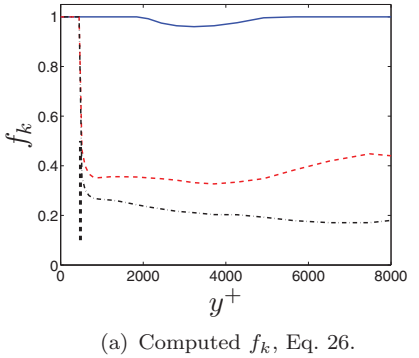

(a) Computed f_k, Eq. 26.

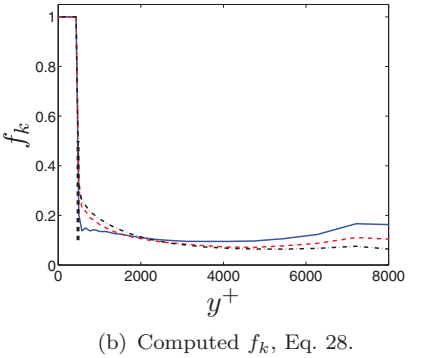

(b) Computed f_k, Eq. 28.

Figure 11. Fully developed channel flow. Computed f_k. $Re_\tau = 8000$. Model 4 is used at the interface. ——: 32^3; – – –: 64^3; – · –: 128^3.

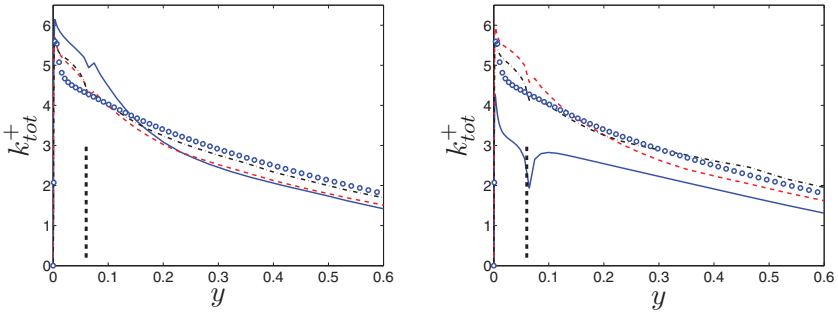

(a) $f_k = 0.4$. (b) Computed f_k.

Figure 12. Fully developed channel flow. $Re_\tau = 8000$. Total, turbulent kinetic energy. Model 4 is used at the interface. ——: 32^3; – –: 64^3; – · –: 128^3; ○: DNS at $Re_\tau = 4\,200$ [42].

It may that Equation (26) – or any other formulation – could be better calibrated, but that is out of the scope of the present work. In this section, we will evaluate the four interface models presented in Section 2.2 in two flows, fully developed channel flows (at different Reynolds numbers) and embedded LES. In the LES region, we set $f_k = 0.4$.

5.1. Fully developed channel flow

Simulations at different Reynolds numbers are made, $Re_\tau = 2000$, $Re_\tau = 4000$ and $Re_\tau = 8000$. The size of the domain is $x_{\max} = 3.2$, $y_{\max} = 2$ and $z_{\max} = 1.6$. The mesh has 32×32 cells in the x–z planes. A simulation with twice as large domain in the x–z plane ($x_{\max} = 6.4$ and $z_{\max} = 3.2$) with 64×64 cells was also made for $Re_\tau = 4000$, and identical results were obtained as for the smaller domain. Details of the grids are given in Table 1. The location of the interface is $y^+ \simeq 500$.

5.1.1. $Re_\tau = 4000$

Figure 13 presents the velocity profiles, the turbulent viscosities, the production terms in the k equation and the shear stresses. The vertical thick dashed lines show the location of the interface. The momentum source in Model 3, S_i (see Equation (22)), is set to zero. Models 2 and 3 give a velocity profile in good agreement with the log law. Model 1 does not sufficiently reduce the turbulent viscosity in the LES region and the result is that the turbulent viscosity is much too large but somewhat smaller than 'no interface model'.

With Model 2, the magnitude of the additional turbulent viscosity, ν_{tr}, near the interface in Figure 13(b) is actually larger than ν_t, which makes their sum, $\nu_t + \nu_{tr}$, go negative. Recall that in the momentum equations, $\nu_t + \nu_{t_{tr}}$ is not allowed to go negative; it is negative only in $P_{k_{tr}}$ (see Section 2.2.1). As a consequence of the large, negative $\nu_{t_{tr}}$ the production term, $P_k + P_{k_{tr}}$, is negative at the interface, see Equation (13 c). The production terms in Models 2 and 3 are very similar, which is expected since ν_{tr} in Model 2 is defined from $P_{k_{tr}}$ (see Equations (17) and (19)). The shear stresses in Figure 13(d) show that without interface condition the flow goes steady. The reason is that the turbulent viscosity in the LES region is too large because there is no commutation term to reduce k. Note that to enhance the readability of Figure 13(d), the viscous and modelled shear stresses are plotted with negative

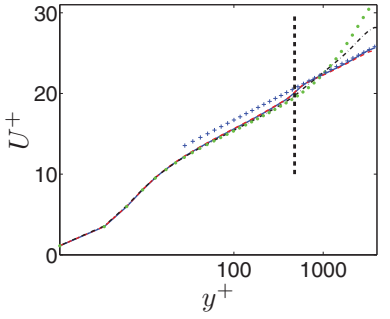

(a) Velocity. +: $U^+ = \ln(y^+)/0.4 + 5.2$

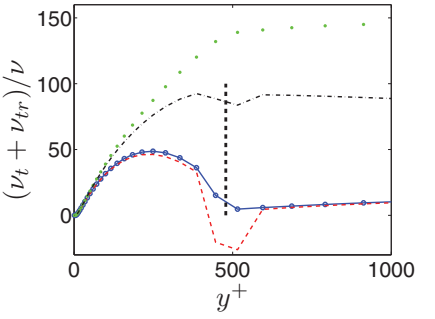

(b) Turbulent viscosity. •: the location of the computational cell centers.

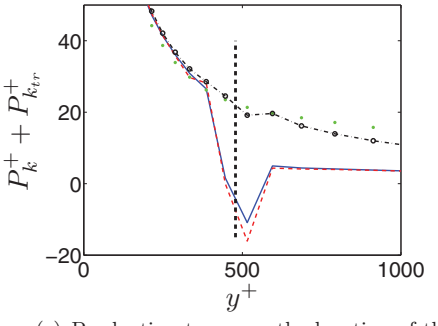

(c) Production terms. •: the location of the computational cell centers.

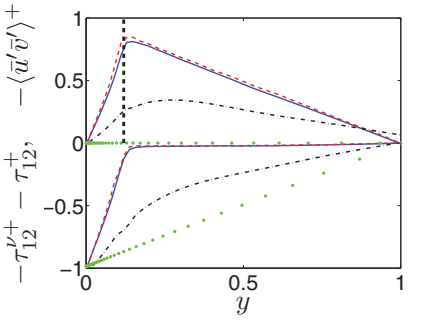

(d) Resolved (upper lines) and viscous plus modeled (lower) shear stresses.

Figure 13. Fully developed channel flow. $N_k = 32$. $Re_\tau = 4000$. ▬·▬: Model 1. ▬ ▬: Model 2. ▬: Model 3, $S_i = 0$; ▬ ▬: no interface model.

sign. Recall that the total shear stress, τ_{tot}, will always – irrespectively of model – obey the linear law:

$$\tau_{\text{tot}} = 1 - y, \quad \tau_{\text{tot}} = \tau_{12}^{\nu} + \tau_{12} - \langle \bar{u}'\bar{v}' \rangle = \langle (\nu + \nu_t) \frac{\partial \bar{u}}{\partial y} - \bar{u}'\bar{v}' \rangle. \tag{30}$$

With Model 1, the flow is neither in RANS mode nor in LES mode, but it ends up in being in the middle (modelled and resolved stresses are both rather large), which is a most unfortunate condition for a hybrid LES–RANS model. The stresses predicted by Models 2 and 3 are virtually identical.

The turbulent viscosity is too large with Model 1 (Figure 13(b)). If f_k is reduced to 0.3, the turbulent viscosity is reduced (not shown) because the gradient of f_k across the interface increases; furthermore, a smaller f_k gives a smaller turbulent viscosity in the LES region which promotes the growth of resolved turbulence. With $f_k = 0.3$, Model 1 gives a velocity profile that is almost identical to that of Model 2; the maximum streamwise fluctuation, $\langle \bar{u}'\bar{u}' \rangle_{\max}$, is 10% larger with Model 1. If f_k is reduced to 0.3 also in Model 2 (not shown), the prediction with the two models is even closer to each other ($\langle \bar{u}'\bar{u}' \rangle_{\max}$ is a couple of per cent larger with $f_k = 0.3$ compared to $f_k = 0.4$).

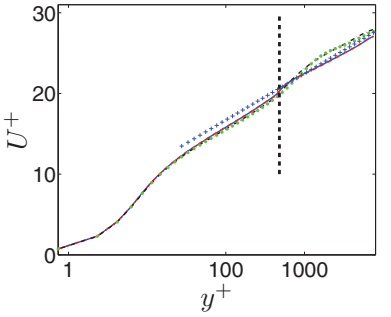

(a) Velocity. +: $U^+ = \ln(y^+)/0.4 + 5.2$

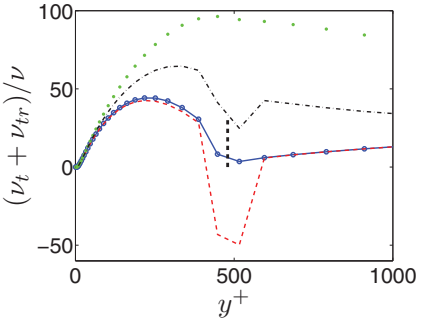

(b) Turbulent viscosity. •: the location of the computational cell centers.

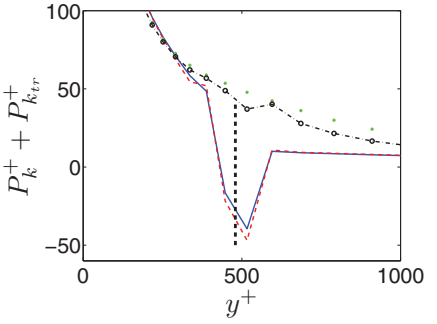

(c) Production term. •: the location of the computational cell centers.

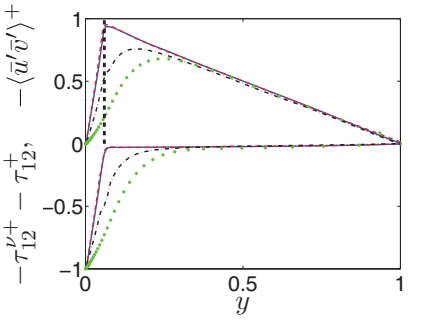

(d) Resolved (upper lines) and viscous plus modeled (lower) shear stresses.

Figure 14. Fully developed channel flow. $Re_\tau = 8000$. For legend, see Figure 13.

5.1.2. $Re_\tau = 8000$

Figure 14 shows the same quantities as Figure 13, but now for $Re_\tau = 8000$. Again, Models 2 and 3 give good velocity profiles. Model 1 and the 'no interface condition' give rather good velocity profiles although the velocity is somewhat too high in the LES region. The reason for the larger velocity levels is seen in Figure 14(b) which presents the turbulent viscosities. The 'no interface model' does not manage to reduce ν_t in the LES region; also Model 1 is much less efficient in reducing ν_t than are Models 2 and 3. This is also clearly seen in the shear stresses (Figure 14(d)) which show that the transition from RANS to LES is fastest for Models 2 and 3; the transition is much slower for Model 1 and for 'no interface condition'. The production of k becomes negative for Models 2 and 3 as for $Re_\tau = 4000$. It can be noted that the magnitude of the negative production at the interface for both $Re_\tau = 4000$ (Figure 13(c)) and $Re_\tau = 8000$ (Figure 14(c)) is slightly larger with Model 2 than Model 3. The reason is probably that Model 2 reduces the turbulent viscosity in the momentum equations by $\nu_{t_{tr}}$ (but its magnitude is not allowed to exceed ν, i.e. $\nu_{tr} > \nu$ when $\nu_{tr} < 0$) which slightly reduces the damping of the resolved fluctuation which in turn increases the fluctuating velocity gradients and the magnitude of P_k. It could be noted that if f_k is reduced to 0.3, Model 1 gives virtually identical velocity profile and resolved stresses as Model 2.

Figure 15 presents results where the momentum source S_i (Equation (22)) has been activated. It can be seen that the predicted velocity profile is slightly worse than without momentum source term (Figure 14(a)). The source terms in the momentum equation are

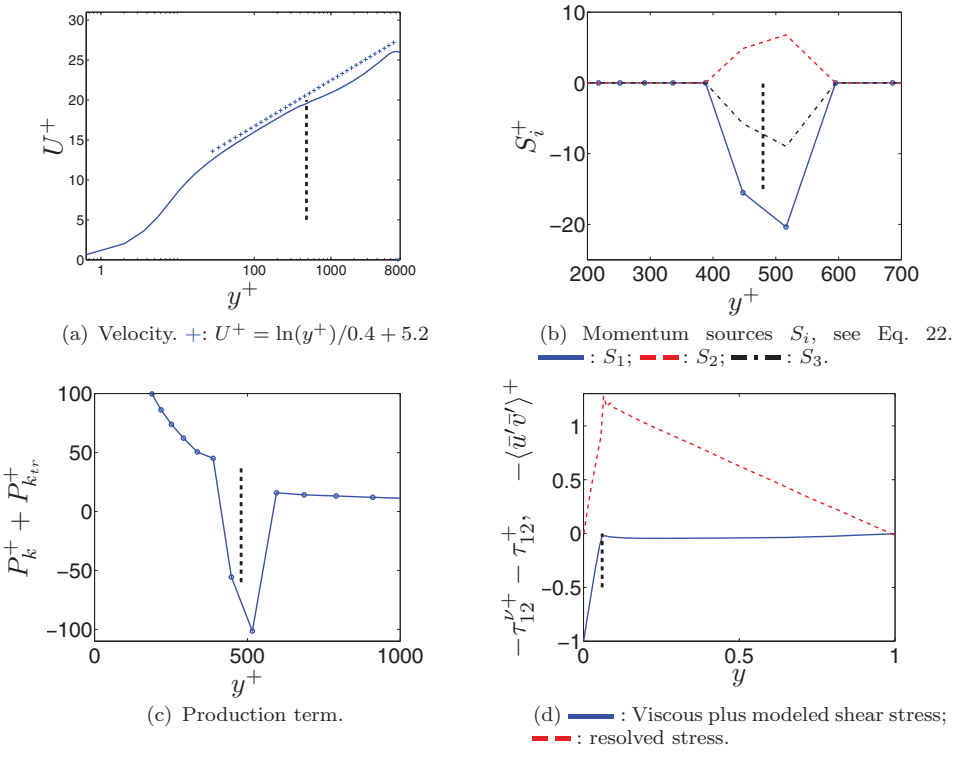

(a) Velocity. +: $U^+ = \ln(y^+)/0.4 + 5.2$

(b) Momentum sources S_i, see Eq. 22. : S_1; : S_2; : S_3.

(c) Production term.

(d) : Viscous plus modeled shear stress; : resolved stress.

Figure 15. Fully developed channel flow. $Re_\tau = 8000$. Model 3. $S_i \neq 0$. • : the location of the computational cell centres. Thick vertical line shows the location of the RANS–LES interface.

- - as is $P_{k_{tr}}$ – very large; recall that the driving pressure gradient (the first term on the right side of Equation (25)) is one. It may at first seem somewhat surprising that the source term S_i is non-zero since it includes the time average of a resolved fluctuation which should be zero, i.e. $\langle u_i' \rangle = 0$. The reason is that S_i, at the lower RANS–LES interface, for example, is added only when $Df_k/Dt = \bar{v}\partial f_k/\partial x_2 < 0$, i.e. when $\bar{v} > 0$ (recall that at the lower RANS–LES interface $\partial f_k/\partial x_2 < 0$); the average of the samples of $\bar{u}_i'$ when $\bar{v} > 0$ is not zero.

It may be noted that the magnitude of the resolved shear stress near the RANS–LES interface exceeds one (see Figure 15(d)) and hence it is larger than the wall shear stress. This seems to violate Equation (30). However, when $S_1 \neq 0$, the right side of Equation (30) includes also the integral of S_1, i.e. the global force balance reads

$$2\delta x_{\max} z_{\max} - 2\tau_w x_{\max} z_{\max} + \int_V S_1 dxdydz = 0 \tag{31}$$

where the first term is the driving pressure gradient (the first term on the right side of Equation (25)). Since $S_1 < 0$ (see Figure 15(b)), the wall shear stress, τ_w, is reduced when S_1 is added and this explains why the magnitude of the resolved shear (scaled with τ_w) exceeds one.

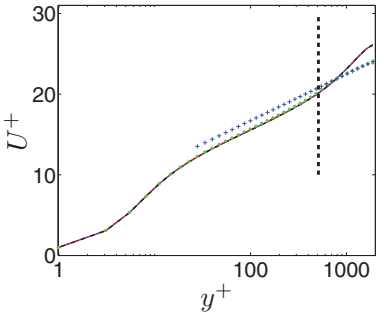

(a) Velocity. +: $U^+ = \ln(y^+)/0.4 + 5.2$

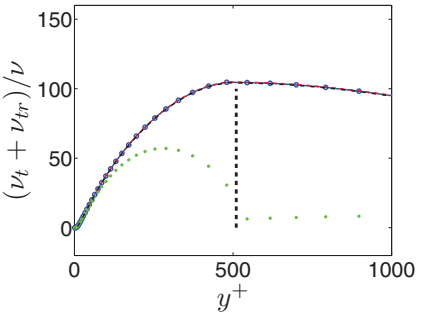

(b) Turbulent viscosity. •: the location of the computational cell centers.

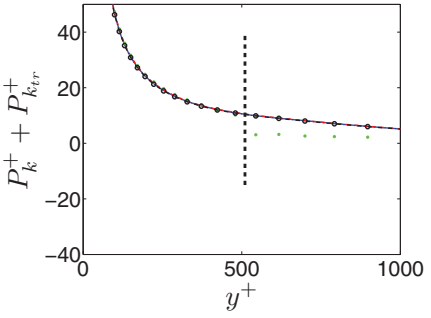

(c) Production term. •: the location of the computational cell centers.

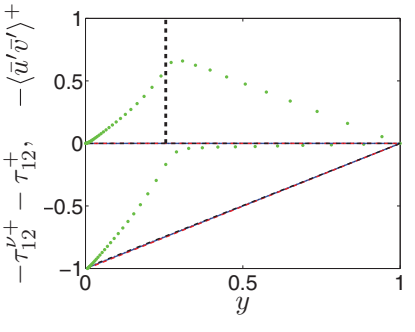

(d) Resolved (upper lines) and viscous plus modeled (lower) shear stresses.

Figure 16. Fully developed channel flow. $Re_\tau = 2000$. – · – · –: Model 1. – – –: Model 2. ——: Model 3, $S_i = 0$; · · · · ·: Model 4.

5.1.3. $Re_\tau = 2\,000$

Figure 16 presents the same quantities as Figure 13, but now for $Re_\tau = 2000$. The results of Model 4 are included here; it was shown in [30] that this interface model gives good results for $Re_\tau = 4000$ and 8000. Model 4 predicts a good velocity profile also for this Reynolds number. However, Models 1–3 fail; they all give a steady RANS solution. The reason is that the interface conditions do not manage to decrease the modelled, turbulent kinetic energy – and hence not the turbulent viscosity – on the LES side of the interface. Obviously, it is more difficult for the flow to switch from RANS to LES at $Re_\tau = 2000$. The same effect is seen if the mesh in the wall-parallel plane is refined to 64 × 64 cells (not shown). One difference between the $Re_\tau = 2\,000$ and the higher Reynolds numbers is that, in the former case, the resolved stress is much smaller at the interface.

5.1.4. Failure of Models 1–3

In order to find the reason for this failure of Models 1–3, the sensitivity to the location of the interface was investigated. Figure 17 presents the velocities, turbulent viscosities and the shear stresses using Model 4 for $Re_\tau = 2000$, 4000 and 8000 for different locations of the interface. The velocity profiles are well predicted for all cases expect for $Re_\tau = 8000$ and $y^+_{\text{interface}} = 250$. Note that the turbulent viscosities are plotted using outer scaling (i.e. they are scaled with friction velocity, u_τ, and half-channel width, δ) contrary to Figures 13–16, where inner scaling is used (i.e. scaled by ν). The results from a 1D RANS simulation using

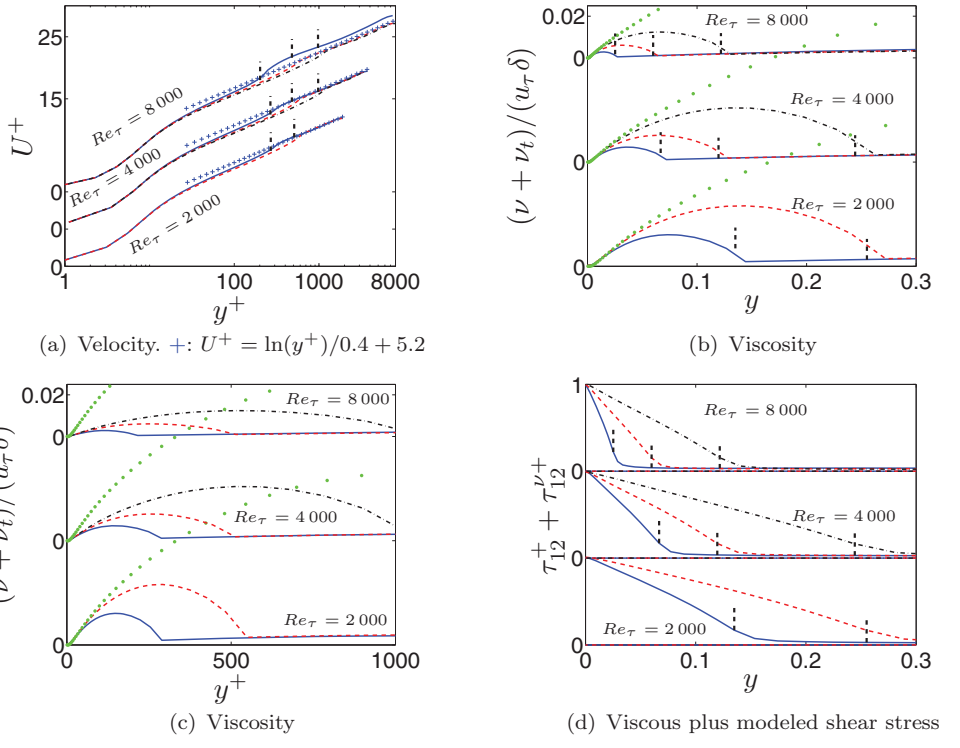

(a) Velocity. +: $U^+ = \ln(y^+)/0.4 + 5.2$ (b) Viscosity

(c) Viscosity (d) Viscous plus modeled shear stress

Figure 17. Fully developed channel flow. Model 4. $Re_\tau = 2000$ (lower lines), $Re_\tau = 4000$ (middle lines), and $Re_\tau = 8000$ (upper lines). Vertical dashed thick lines show the location of the interfaces. ——: $y^+_{\text{interface}} = 250$; – – –: $y^+_{\text{interface}} = 500$; – · – · –: $y^+_{\text{interface}} = 1000$; ——: 1D RANS using AKN model.[45]

the AKN model [45] (i.e. PANS with $f_k = 1$) are also included. When plotted versus y^+, the RANS turbulent viscosity is virtually independent of Reynolds number and hence all the green dotted lines in Figure 17(c) collapse. Actually, this is also the case for the PANS simulations when the interface is defined in outer scaling (i.e. in y): in Figure 17(b), the turbulent viscosity in the URANS region for

- $\{Re_\tau = 2000, y^+_{\text{interface}} = 250\}$, and $\{Re_\tau = 4000, y^+_{\text{interface}} = 500\}$ and $\{Re_\tau = 8000, y^+_{\text{interface}} = 1000\}$ (i.e. $y = 0.125$)
- $\{Re_\tau = 2000, y^+_{\text{interface}} = 500\}$, and $\{Re_\tau = 4000, y^+_{\text{interface}} = 1000\}$ (i.e. $y = 0.25$)
- $\{Re_\tau = 4000, y^+_{\text{interface}} = 250\}$, and $\{Re_\tau = 8000, y^+_{\text{interface}} = 500\}$ (i.e. $y = 0.0625$)

is very similar. As a result, this applies also for the viscous plus modelled shear stresses (see Figure 17(d)). It is interesting to note that the viscosity in the RANS region in the PANS simulations is much smaller than that in the 1D RANS simulation. The reason is, as noted in [30], that low modelled k values are transported from the LES region into the RANS region near the lower wall when $\nu' < 0$ (ε in the LES region in the two simulations are very similar [30]).

Now we need to address the question why Models 1–3 fail at $Re_\tau = 2000$. The interface location was moved away from the wall to $y^+_{\text{interface}} \simeq 1000$, but the same results were obtained (not shown). Next, the interface location was moved closer to the wall, to $y^+_{\text{interface}} \simeq 250$. Model 1–3 still fail to predict a good velocity profile (not shown). It was

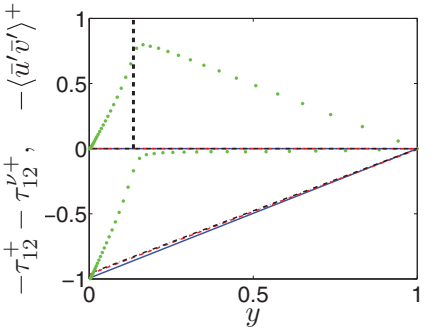

Figure 18. Fully developed channel flow. $Re_\tau = 2000$, $y^+_{\text{interface}} = 250$. Resolved (upper lines) and viscous plus modelled (lower) shear stresses. For legend, see Figure 15.

mentioned above that the reason for the poor prediction of the velocity profile at $Re_\tau = 2000$ could be that the resolved shear stress is too low at the interface, and that the low level of resolved turbulence in the interface region would make the transition from RANS mode to LES mode difficult. However, this theory does not hold when we look at the resolved shear stresses at the interface in Figure 18 which for $Re_\tau = 2000$ are as large or larger than those at $Re_\tau = 8000$ for which good velocity profiles are obtained (see Figure 14). The reason for the poor prediction at $Re_\tau = 2000$ is that the turbulent viscosity (in outer scaling) – and, consequently, the modelled shear stress – is much larger than at the higher Reynolds number (see Figure 17(b)–(d)). Because of this, Models 1–3 do not manage to sufficiently decrease ν_t in the LES region adjacent to the interface. Large modelled shear stresses at the interface (Figure 17(d)) are also the reason for the somewhat poorly predicted velocity profiles (Figure 17(a)) – using Model 4 – at $Re_\tau = 4000$ and 8000 with the interface located at $y^+ = 250$.

5.2. Embedded LES of channel flow

The Reynolds number is $Re_\tau = u_\tau \delta/\nu = 950$. The domain size is $12.8 \times 2 \times 1.6$ in the streamwise (x), wall-normal (y) and spanwise directions (z) (see Figure 17). The mesh has $256 \times 80 \times 64$ cells. A geometrical stretching of 1.13 in the y direction is used from the walls to the centre.

Anisotropic synthetic fluctuations are superimposed to the mean flow profiles at the inlet. The methodology used in [28,47] is somewhat extended and involves the following steps.

(1) A precursor 1D RANS simulation is made using the AKN model [45] (i.e. PANS with $f_k = 1$).
(2) The Reynolds stress tensor is computed using the EARSM model.[48]
(3) The Reynolds stress tensor is used as input for generating the anisotropic synthetic fluctuations.
(4) Since the method of synthetic turbulence fluctuations assumes homogeneous turbulence, we can only use the Reynolds stress tensor in one point. We need to chose a relevant location for the Reynolds stress tensor. In boundary layer flow, the turbulent shear stress is the single most important stress component. Hence, the Reynolds

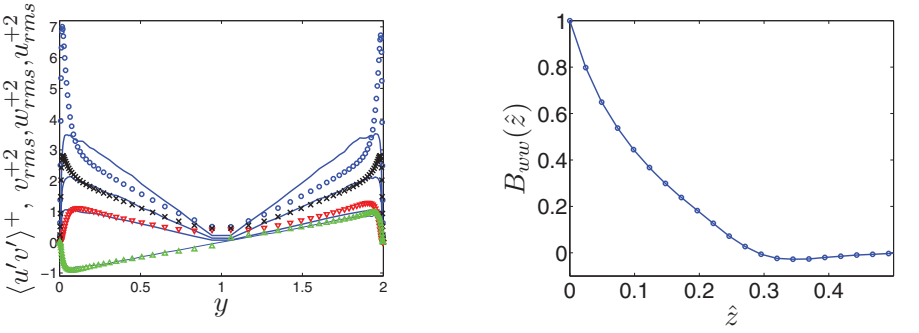

(a) Reynolds stresses. Markers: EARSM. △: $\langle u'v' \rangle^+$; ▽: u^{+2}_{rms}; ×: w^{+2}_{rms}; ○: u^{+2}_{rms}

(b) Two-point correlation. Markers denote location of cell centers.

Figure 19. Embedded LES. Channel flow. Added synthetic Reynolds stresses at the vertical RANS–LES interface.

stress tensor is taken at the location where the magnitude of the turbulent shear stress is the largest.

(5) Finally, the synthetic fluctuations are scaled with

$$\left(|\overline{u'v'}|/|\overline{u'v'}|_{\max}\right)^{1/2}_{\text{RANS}}, \tag{32}$$

which is taken from the 1D RANS simulation.

In order to introduce a time correlation, the inlet fluctuations, $\mathcal{U}'$, are computed as

$$\mathcal{U}'_m = a\mathcal{U}'_{m-1} + bu'_m, \tag{33}$$

where m is the current time step. Constant a is related to the integral timescale, $\mathcal{T}$, as

$$a = \exp(-\Delta t/\mathcal{T}), \tag{34}$$

where Δt is the computational time step and $b = (1 - a^2)^{1/2}$. Constant b is given by the requirement that $\langle \mathcal{U}'^2 \rangle = \langle u'^2 \rangle$. Equation (33) introduces a time correlation with an integral timescale $\mathcal{T}$ which is taken as $\mathcal{T} = \mathcal{L}/U_b$ ($\mathcal{L} = 0.15\delta$) using Taylor's hypothesis, where U_b and $\mathcal{L}$ denote the inlet bulk velocity and the integral length scale, respectively.

The inlet mean velocities are set as $V_{in} = W_{in} = 0$ and [49]

$$U^+_{in} = \begin{cases} y^+ & y^+ \leq 5 \\ -3.05 + 5\ln(y^+) & 5 < y^+ < 30 \\ \frac{1}{0.4}\ln(y^+) + 5.2 & y^+ \geq 30. \end{cases} \tag{35}$$

The time-averaged interface fluctuations and the two-point correlation of w' are shown in Figure 19. It can be noted in Figure 19 that the sign of the shear stress changes at the centreline. This was achieved by simply switching the sign of the wall-normal synthetic fluctuation, v', for $y > 1$. It can be seen that the variation of all the synthetic stresses across the channel follow the form of the eddy viscosity shear stress (which is more or less identical

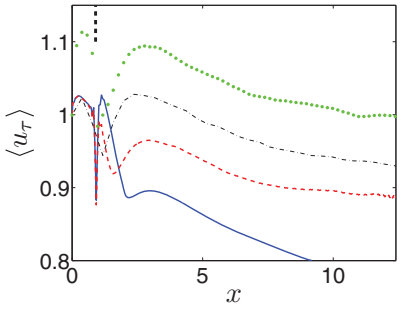

(a) Friction velocity. : $x_{tr} = 0$ with inlet profile from PANS.

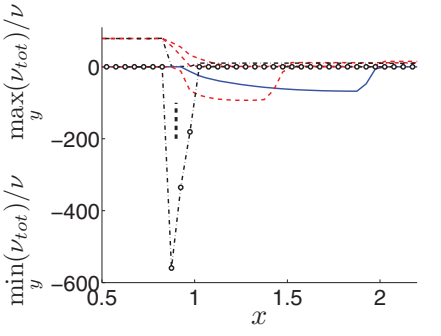

(b) Minimum (lower lines) and maximum (upper lines) turbulent viscosity. Markers denote location of cells centers.

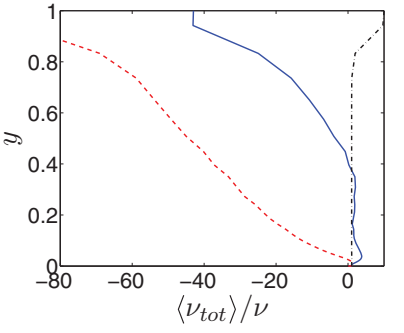

(c) Turbulent viscosity. $x = 1.18$

Figure 20. Embedded LES. Friction velocity and turbulent viscosity ($\nu_{\text{tot}} = \nu + \nu_t + \nu_{tr}$). Model 2. Black, thick, vertical dashed lines show the location of the interface. : $x_{tr} = 1$; : $x_{tr} = 0.5$; : $x_{tr} = 0$ (see Figure 12).

to the EARSM shear stress). The reason is that Equation (32) was used to scale all fluctuations. As a consequence, the synthetic normal stresses agree with the EARSM stresses at the location where the EARSM shear stress has its maximum. When creating the synthetic turbulent interface fluctuations, the integral length scale was set to 0.15δ. Figure 19(b) shows that the two-point correlation of the generated fluctuations agrees well with this value. A MATLAB file to generate the synthetic fluctuations can be downloaded at [50]. RANS is used upstream of the interface ($f_k = 1$) and LES is used downstream of it ($f_k = 0.4$) and in the transition region of length x_{tr} (see Figure 17), f_k varies linearly between 1 and 0.4. Models 1–4 are used at the vertical interface.

We start by investigating the effect of the length of the transition region. Figure 20 presents the turbulent viscosities for three different transition lengths, $x_{tr} = 0$, 0.5 and $x_{tr} = 1$. Model 2 is used at the interface. A large x_{tr} means that the gradient Df_k/Dt in Equation (9) is small but that it is active over a large region. We see immediately in Figure 20(a) that $x_{tr} = 1$ is too large. The skin friction does not go back to its target value of one downstream of the interface because the resolved turbulence is much too small (not shown). Reducing x_{tr} to 0.5 gives an improvement but the transition region is still too long. $x_{tr} = 0$ (no transition region, f_k goes from 1 to 0.4 abruptly) gives good friction velocities; the fully developed values of $u_\tau \simeq 0.95$ is reached at $x \simeq 10$, i.e. nine half-channel widths downstream of the

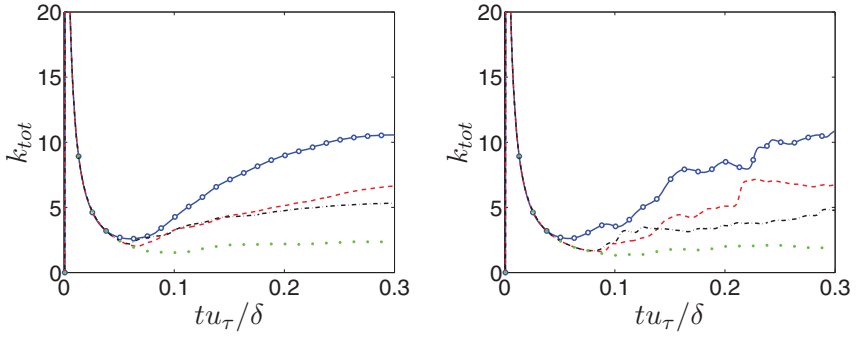

(a) Running average in z and t (b) Running average in t

Figure 21. Embedded LES. Model 2. Running average (Equation (20)) in a computational cell at $(x/\delta, z/\delta) = (2.42, 0.8)$. ——: $y/\delta = 0.014$; – –: $y/\delta = 0.065$; – · –: $y/\delta = 0.24$; · · ·: $y/\delta = 0.83$; ○: every 20th time step.

interface. The reason why the friction velocity does not reach the target value of one is that the resolution is somewhat too coarse (or the Reynolds number too high) so that the velocity profile for fully developed PANS does not agree with the inlet log-law profile in Equation (35) (see Figure 11a in [27]). When the inlet mean velocity instead is taken from fully developed flow on the same mesh using PANS (with $f_k = 0.4$), the friction velocity goes to one as expected (see green dotted line in Figure 20(a)).

Figure 20(b) and 20(c) shows that the turbulent viscosity takes negative values for all transition region lengths, which gives negative production in the k equation; the smaller the transition region, the larger the magnitude of the negative viscosity. With no transition region ($x_{tr} = 0$), it can be seen that the magnitude of ν_{tot} gets very large downstream of the interface ($|\nu_{\text{tot}}|/\nu > 550$). Despite the large negative viscosities adjacent to the RANS–LES interface, they rapidly get back to positive values as seen in Figure 20(c) which show the turbulent viscosities five cells downstream of the interface. Since $x_{tr} = 0$ is found to give the best results earlier, this choice is used when presenting the results in more detail later.

In Models 2 and 3, a running average is used for computing k_{tot} (see Equation (20)). The running average is applied at the start of the simulations. Figure 21 shows how fast the running average converges. The inlet conditions are used as initial conditions in the entire computational domain. Figure 21(a) shows that the running average converges fairly well within 0.1 time units. One test was also made where the running average was made only in time, not in the spanwise direction. In this case, ν_{tr} in Equation (17) was set to zero during the first 10 time steps in order to get some reasonable value of k_{tot} in Equation (20). Figure 21(b) shows the convergence of the running average, and as can be seen, it converges fairly quickly but slightly slower than in Figure 21(a). The predicted results (not shown) using the two different running averages in Figure 21(a) and 21(b) are identical.

Figures 22 and 23 present velocity profiles, resolved turbulence, friction velocity and turbulent viscosity. The momentum source, S_i (Equation (22)), is set to zero. First, it can be seen that with Model 1, too small a part of the resolved turbulence survives in the LES region because it is killed by the large turbulent viscosity. The friction velocity (Figure 23(a)) is the most critical parameter. Models 2–4 give very similar u_τ for $x > 5$ and reach their fully developed values at $x \simeq 10$. The velocity profile and resolved turbulence are also fairly well

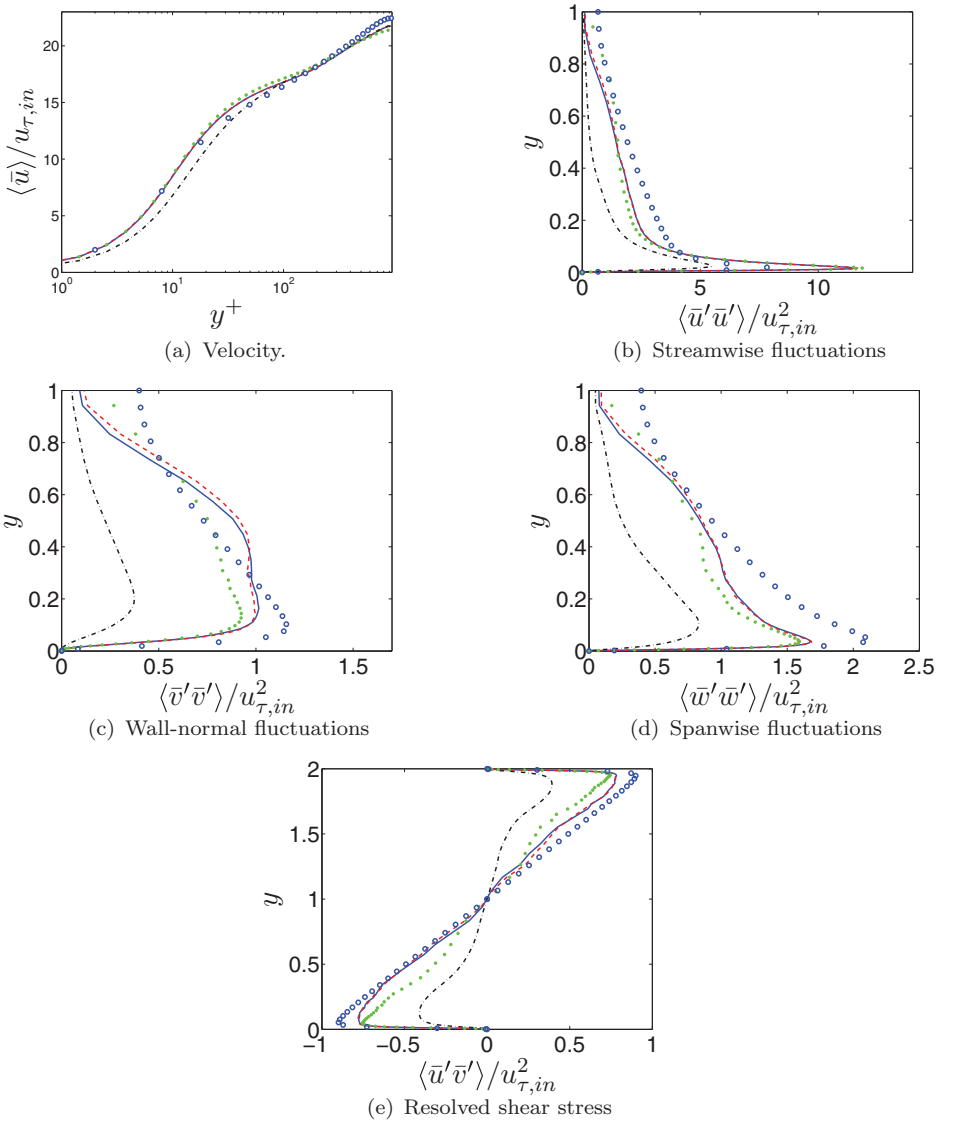

Figure 22. Embedded LES. $x = 5.9$. $Re_\tau = 950$. $x_{tr} = 0.5$. ▬·▬·▬ : Model 1; ▬ ▬ : Model 2; ▬▬ : Model 3, $S_i = 0$; ▬ ▬ : Model 4; ○ : DNS of fully developed flow.[46]

predicted at $x = 5.9$ (i.e. five half-channel widths downstream the interface; see Figure 22). In the case of Model 1, the resolved turbulence further downstream ($x \gg 6.4$) will probably be completely killed first and then the flow will eventually go into RANS mode. With Models 2–4, the resolved turbulence at the interface increases strongly (Figure 23(b)), thanks to the added non-isotropic fluctuations, but also thanks to interface conditions of Models 2–4 which succeed in drastically decreasing the modelled turbulent kinetic energy and thereby the turbulent viscosity (see Figure 23(c)). For Models 1 and 2, the reduction in the turbulent viscosity is clearly seen in Figure 23(d). Model 2 gives a much larger magnitude in negative viscosity than Model 1 and as a consequence the turbulent viscosity for Model 2 is zero for $y < 0.8$ at $x = 5.9$ (see Figure 23(e)).

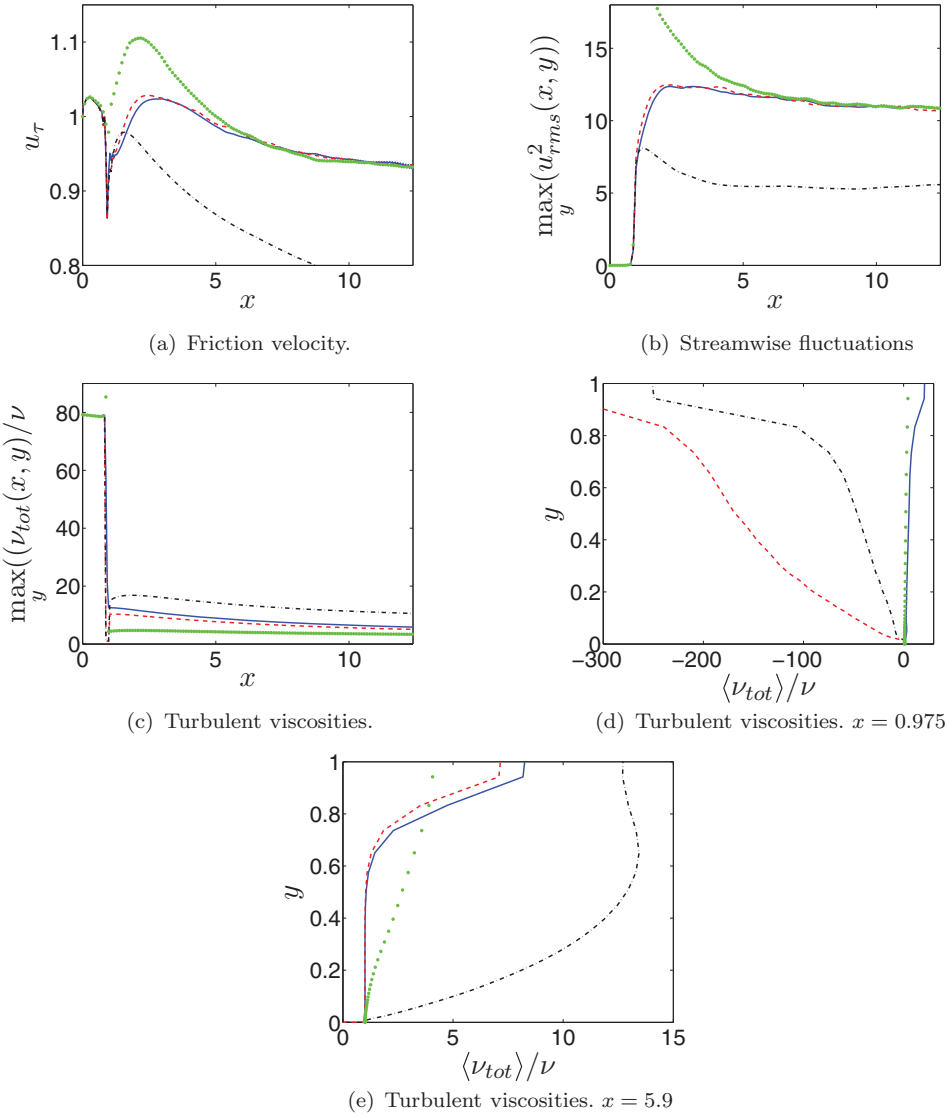

(a) Friction velocity.

(b) Streamwise fluctuations

(c) Turbulent viscosities.

(d) Turbulent viscosities. $x = 0.975$

(e) Turbulent viscosities. $x = 5.9$

Figure 23. Embedded LES. $Re_\tau = 950$. $x_{tr} = 0$. $\nu_{tot} = \nu + \nu_t + \nu_{tr}$. For legend, see Figure 22.

For the fully developed channel flow at $Re_\tau = 4000$, it was found that when f_k was reduced to 0.3 using Model 1 (see Section 5.1.1), the predictions were found to be very similar to those of Model 2. When f_k is reduced to 0.3 for this flow with Model 1, the results improve somewhat (not shown), but they are still considerably poorer compared with Model 2. The skin friction reaches a value of 0.9 near the outlet of the domain (cf. Figure 23(b)) and the peak of the resolved shear stress is approximately 0.5 (cf. Figure 22(e)) near the outlet of the domain. The reason is that the turbulent viscosity at $x = 5.9$ is reduced only by a factor of two compared to $f_k = 0.4$ (cf. Figure 23(d)).

The production of k in the LES region adjacent to the RANS–LES interface is shown in Figure 24. As for the fully developed channel flow, it is found that the productions by the

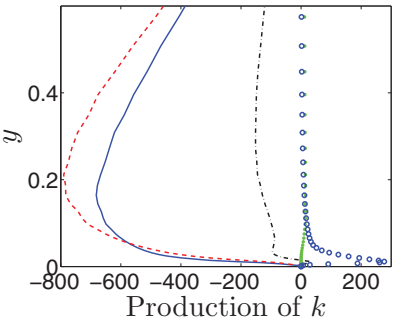

Figure 24. Embedded LES. $Re_\tau = 950$. $x_{tr} = 0$. Production in the plane in the LES region adjacent to the interface. ▬·▬·▬ : $P_k + P_{k_{tr}}$, Model 1. ▬ ▬ : $P_k + P_{k_{tr}}$, Model 2. ▬▬ : $P_{k_{tr}}$, Model 3, $S_i = 0$; ····· : P_k, Model 4; ○ : P_k in RANS region, $x = 0.12$.

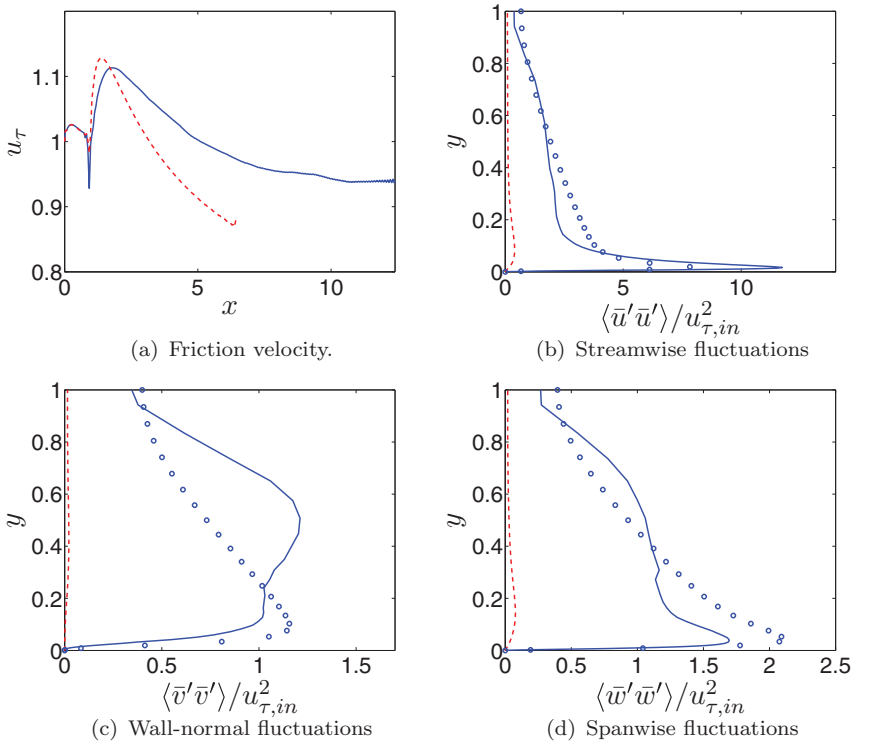

Figure 25. Embedded LES. $x = 5.9$. $Re_\tau = 950$. $x_{tr} = 0$. ▬▬ : Model 3. $S_i \neq 0$ (see Equation (22)); ▬ ▬ : no interface model; ○ : DNS of fully developed flow.[46]

interface models, $P_{k_{tr}}$, are very large and negative for Models 2 and 3. These large negative productions ensure the strong decrease in turbulent viscosity across the RANS–LES interface (see Figure 23(d)), which in turn facilitates the rapid increase in resolved turbulence downstream of the interface (see Figure 23(b)).

Figure 25 presents results using Model 3 with the momentum source term, S_i (see Equation (22)(. Comparing with Figure 22, we can see that the momentum source has a similar

influence as for fully developed flow: the resolved turbulence is slightly stronger. The predicted friction is as a consequence increased and somewhat closer to the target value of one.

Figure 25 includes also results when no interface model is used at all. When comparing with the results when using an interface model (Figure 22), the differences are clear: without interface model, the turbulent viscosity is not reduced on the LES side of the interface and the consequence is that almost all resolved turbulence are killed. If the domain in Figure 25 were made larger in the streamwise direction, the flow would surely return to steady RANS further downstream.

6. Conclusions

Simulations using zonal PANS are made where $f_k = 1$ in the URANS region and $f_k = 0.4$ in the LES region. There is a a strong gradient of f_k across the RANS–LES interface. Recently, a modification of the PANS model was proposed by Girimaji and Wallin [3] where they take the gradient of f_k into account. This approach is used at the RANS–LES interfaces and it is further developed and evaluated in the present work. Four different treatments of the interface are evaluated; one is the approach proposed in [3] (called Model 1). Models 2 and 3 are modifications of Model 1, and Model 4 is the approach presented in [30]. The beauty of Models 1–3 is that they do not depend on any constants or tuning; they use the gradient of f_k across the interface. The advantage of Model 3 is that it – unlike Models 1 and 2 – does not involve any unphysical negative viscosities and does not require any regularisation. The disadvantage of Model 4 is that it depends on how the modelled k and ε are treated at the interface. The four models are evaluated in fully developed channel flow and embedded LES in channel flow.

Before evaluating the different interface models, the paper evaluates different ways to prescribe f_k. Two different ways of computing f_k are employed (Equations (26) and (28)). In the third option a constant f_k is used ($f_k = 0.4$). The three different options are evaluated for decaying grid turbulence and fully developed channel flow, and it is found that the best option is to use a constant $f_k = 0.4$.

Model 1 does not give good results. Its effect is too weak and the model does not sufficiently decrease the turbulent viscosity on the LES side of the interface. For fully developed channel flow, it works well if f_k is reduced to 0.3. For embedded LES, a reduction of f_k to 0.3 in Model 1 improves the predictions, but Model 1 still performs much worse than Model 2.

Models 2 and 3 give mostly good results and virtually identical results. Model 3 includes an additional production term, $P_{k_{tr}}$, and a source term in the momentum equations, S_i (Equation (22)); it is found that it is preferable to set $S_i = 0$. To make Models 1 and 2 numerically stable, the additional turbulent viscosity, $\nu_{t_{tr}}$, from the models must be positive in the momentum equations. In the production term in the k equation, $\nu_{t_{tr}}$ is permitted to go negative. The magnitude of the negative added production, $P_{k_{tr}}$, in Models 2 and 3 is much larger than the ordinary P_k in RANS. This is the key to the success: $P_{k_{tr}}$ is large and negative in the LES region adjacent to the interface which reduces k and thereby the turbulent viscosity. Models 2 and 3 fail for the fully developed flow at the lowest Reynolds number ($Re_\tau = 2000$); they both give steady RANS results. Model 4 works well for all flows.

In fully developed channel flow using RANS, the turbulent viscosity, and hence the modelled Reynolds shear stress, is virtually independent of the Reynolds number. Using zonal

PANS, it is found that this also applies for the turbulent viscosity and the modelled Reynolds shear stress in the URANS region.

The conclusion is that interface Model 4 works best and that Models 2 and 3 fail in one flow (fully developed channel flow at $Re_\tau = 2000$). The disadvantage of Model 4 is that it depends on the prescribed boundary conditions of k and ε at the RANS–LES interface.

Disclosure statement

No potential conflict of interest was reported by the author.

References

[1] Girimaji SS. Partially-averaged Navier–Stokes model for turbulence: a Reynolds-averaged Navier–Stokes to direct numerical simulation bridging method. ASME J Appl Mech. 2006; 73(2): 413–421.

[2] Basara B, Krajnović S, Girimaji S, et al. Near-wall formulation of the partially averaged Navier–Stokes turbulence model. AIAA J. 2011; 49(12): 2627–2636.

[3] Girimaji SS, Wallin S. Closure modeling in bridging regions of variable-resolution (VR) turbulence computations. J Turbul. 2013;14(1):72–98.

[4] Spalart PR, Jou W-H, Strelets M, et al. Comments on the feasability of LES for wings and on a hybrid RANS/LES approach. In: Liu C, Liu Z, editors. Advances in LES/DNS. First AFOSR International Conference on DNS/LES; Louisiana Technical University; Columbus (OH): Greyden Press; 1997.

[5] Spalart PR. Strategies for turbulence modelling and simulations. Int J Heat Fluid Flow. 2000; 21: 252–263.

[6] Shur ML, Spalart PR, Strelets K.M., et al. A hybrid RANS–LES approach with delayed-DES and wall-modelled LES capabilities. Int J Heat Fluid Flow. 2008; 29: 1638–1649.

[7] Davidson Lars, Peng Shia-Hui. *Hybrid LES-RANS: a one-equation SGS model combined with a k–ω for predicting recirculating flows*. Int J Numer Methods Fluids. 2003; 43(9): 1003–1018.

[8] Temmerman L, Hadiabdi M, Leschziner MA, et al. A hybrid two-layer URANS–LES approach for large eddy simulation at high Reynolds numbers. Int J Heat Fluid Flow. 2005; 26(2): 173–190.

[9] Menter FR, Egorov Y. The scale adaptive simulation method for unsteady turbulent flow predictions. Part 1: Theory and description. Flow Turbul Combust. 2010; 85: 113–138.

[10] Egorov Y, Menter FR, Lechner R, et al. The scale adaptive simulation method for unsteady flow predictions. Part 2: Application to complex flows. Flow Turbul Combust. 2010; 85: 139–165.

[11] Fröhlich J, von Terzi D. Hybrid LES/RANS methods for the simulation of turbulent flows. Prog Aerosp. 2008; 44(5): 349–377.

[12] Travin A, Shur M, Strelets M, et al. Detached-eddy simulations past a circular cylinder. Flow Turbul Combust. 2000; 63(1/4): 293–313.

[13] Kok JC, Dol HS, Oskam B, et al. Extra-large eddy simulation of massively separated flows. AIAA paper 2004-264; 2004; Reno, NV.

[14] Davidson L, Billson M. Hybrid LES/RANS using synthesized turbulence for forcing at the interface. Int J Heat Fluid Flow. 2006; 27(6): 1028–1042.

[15] Schiestel R, Dejoan A. Towards a new partially integrated transport model for coarse grid and unsteady turbulent flow simulations. Theor Comput Fluid Dyn. 2005; 18(6): 443–468.

[16] Chaouat B, Schiestel R. A new partially integrated transport model for subgrid-scale stresses and dissipation rate for turbulent developing flows. Phys Fluids. 2005;17(065106).

[17] Menter FR, Schütze J, Kurbatskii KA, et al. Scale-resolving simulation techniques in industrial CFD. 6th AIAA Theoretical Fluid Mechanics Conference, AIAA paper 2011-3474; 2011 June 27–30; Honolulu, HI.

[18] Mathey F, Cokljat D, Bertoglio JP, et al. Assessment of the vortex method for large eddy simulation inlet conditions. Prog Comput Fluid Dyn. 2006; 6(1–3): 58–67.

[19] Shur ML, Spalart PR, Strelets MK, et al. A rapid and accurate switch from RANS to LES in boundary layers using an overlap region. Flow Turbul Combust. 2011; 86(2): 179–206.
[20] Poletto R, Revell A, Craft T, et al. Embedded DDES of 2D hump flow. In: Song F, Werner H, Shia-Hui P, Dieter S, editors. Progress in hybrid RANS–LES modelling. Vol. 117, Notes on numerical fluid mechanics and multidisciplinary design. Berlin: Springer-Verlag; 2012. p. 169–179, 314. Available from: http://dx.doi.org/10.1007/978-3-642-31818-4_26.
[21] Poletto R, Craft T, Revell A. A new divergence free synthetic eddy method for the reproduction of inlet flow conditions for LES. Flow Turbul Combust 2013;91:519–539.
[22] Gritskevich M, Garbaruk A, Schütze J, et al. *Development of DDES and IDDES formulations for the k–ω shear stress transport model*. Flow Turbul Combust. 2012; 88: 431–449.
[23] Adamian A, Travin A. An efficient generator of synthetic turbulence at RANS-LES interface in embedded LES of wall-bounded and free shear flows. In: Kurzmin A, editor. Proceedings of Sixth International Conference on Computational Fluid Dynamics, ICCFD6; 2010 Jul 12–16; Berlin: Springer-Verlag; 2011. p. 739–744.
[24] Shur M, Spalart PR, Strelets MK, et al. Synthetic turbulence generators for rans-les interfaces in zonal simulations of aerodynamic and aeroacoustic problems. Flow Turbul Combust. 2014; 93: 69–92.
[25] Xiao H, Jenny P. A consistent dual-mesh framework for hybrid LES/RANS modeling. J Comput Phys. 2012; 231: 1848–1865.
[26] Deck S. Recent improvements in the zonal detached eddy simulation (ZD) formulation. Theoretical Comput Fluid Dyn. 2012;26(6):523–550. ISSN 0935-4964. Available from: http://dx.doi.org/10.1007/s00162-011-0240-z.
[27] Ma J, Peng S-H, Davidson L, et al. A low Reynolds number variant of Partially-Averaged Navier–Stokes model for turbulence. Int J Heat Fluid Flow. 2011;32(3):652–669. Available from: http://dx.doi.org/10.1016/j.ijheatfluidflow.2011.02.001.
[28] Davidson L, Peng S-H. Embedded large-eddy simulation using the partially averaged Navier-Stokes model. AIAA J. 2013;51(5):1066–1079. Available from: http://dx.doi.org/10.2514/1.J051864.
[29] Davidson L. Large eddy simulation of heat transfer in boundary layer and backstep flow using PANS. In: Hanjalić K, Nagano Y; Jakirlić S, editors. Turbulence, Heat and Mass Transfer, THMT-12, Palermo, Sicily/Italy; 2012 Sep 24–27; Redding (CT): Begell House Inc.; 2012. (Corrected version can be downloaded at http://www.tfd.chalmers.se/˜lada/.)
[30] Davidson L. The PANS k–ε model in a zonal hybrid RANS-LES formulation. Int J Heat Fluid Flow. 2014;46:112–126. Available from: http://dx.doi.org/10.1016/j.ijheatfluidflow.2014.01.002.
[31] Hamba F. Analysis of filtered Navier-Stokes equation for hybrid RANS/LES simulation. Phys Fluids A. 2011; 23: 015108.
[32] Chaouat B, Schiestel R. Partially integrated transport modeling method for turbulence simulation with variable filters. Phys Fluids. 2013; 25: 125102.
[33] Davidson L. Two-equation hybrid RANS-LES models: a novel way to treat k and ω at the inlet. In: Hanjalić K, Miyauchi T, Borello D, Hadiabdić M, Venturini P, editors. Turbulence, Heat and Mass Transfer, THMT-15, Sarajevo, Bosnia and Herzegovina; 2015 Sep 15–18; New York: Begell House Inc.; 2015.
[34] Peng S-H, Davidson L, Holmberg S. *A modified low-Reynolds-number k–ω model for recirculating flows*. J Fluids Eng. 1997; 119: 867–875.
[35] Travin A, Shur M, Strelets M, Spalart P. Detached-eddy simulations past a circular cylinder. Flow Turbul Combust. 2000; 63: 293–313.
[36] Versteegh HK, Malalasekera W. An introduction to computational fluid dynamics – the finite volume method. Harlow: Longman Scientific & Technical; 1995.
[37] van Leer B. Towards the ultimate conservative difference scheme. Monotonicity and conservation combined in a second order scheme. J Comput Phys. 1974; 14(4): 361–370.
[38] Kenjeres S, Hanjalic K. LES, T-RANS and hybrid simulations of thermal convection at high ra numbers. Int J Heat Fluid Flow. 2006; 27: 800–810.

[39] Germano M, Piomelli U, Moin P, et al. A dynamic subgrid-scale eddy viscosity model. Phys Fluids A. 1991; 3: 1760–1765.
[40] Lilly DK. A proposed modification of the Germano subgrid-scale closure method. Phys Fluids A. 1992; 4: 633–635.
[41] Comte-Bellot G, Corrsin S. Simple Eularian time correlation of full- and narrow-band velocity signals in grid-generated 'isotropic' turbulence. J Fluid Mech. 1971; 48(2): 273–337.
[42] Lozano-Duran A, Jimenez J. Effect of the computational domain on direct simulations of turbulent channels up to $Re_\tau = 4200$. Phys Fluids A. 2014; 26: 011702.
[43] Girimaji SS, Abdol-Hamid KS. Partially-averaged Navier–tokes model for turbulence: implementation and validation. AIAA Paper 2005-0502, Reno, NV; 2005.
[44] Foroutan H, Yavuzkurt S. A partially-averaged Navier–Stokes model for the simulation of turbulent swirling flow with vortex breakdown. Int J Heat Fluid Flow. 2014; 50: 402–416.
[45] Abe K, Kondoh T, Nagano Y. A new turbulence model for predicting fluid flow and heat transfer in separating and reattaching flows – 1. Flow field calculations. Int J Heat Mass Transfer. 1994;37(1):139–151.
[46] Hoyas S, Jimenez J. Reynolds number effects on the reynolds-stress budgets in turbulent channels. Phys Fluids A. 2008;20(101511). Available from: http://torroja.dmt.upm.es/channels/.
[47] Davidson L. Using isotropic synthetic fluctuations as inlet boundary conditions for unsteady simulations. Adv Appl Fluid Mech. 2007; 1(1): 1–35.
[48] Wallin S, Johansson AV. A new explicit algebraic Reynolds stress model for incompressible and compressible turbulent flows. J Fluid Mech. 2000; 403: 89–132.
[49] Welty JR, Wicks CE, Wilson RE. Fundamentals of momentum, heat, and mass transfer. 3rd ed. New York: John Wiley & Sons; 1984.
[50] Davidson L. How to implement synthetic inlet boundary conditions. Available from: http://www.tfd.chalmers.se/~lada/projects/inlet-boundary-conditions/proright.html, 2013.